Nonlinear thermo-elastic phase-field fracture of thin-walled structures relying on solid shell concepts

P K Asur Vijaya Kumar[a,c], A. Dean[b,c], J. Reinoso[c,*], M. Paggi[a]

[a]*IMT School for Advanced Studies Lucca, Piazza San Francesco 19, 55100, Lucca, Italy*
[b]*School of Civil Engineering, College of Engineering, Sudan University of Science and Technology, P.O. Box 72, Khartoum, Sudan*
[c]*Elasticity and Strength of Materials Group, School of Engineering, University of Seville, Camino de los Descubrimientos s/n, 41092, Seville, Spain*

Abstract

The analysis of fracture phenomena of thin-walled structures has been a matter of intensive research in the last decades. These phenomena notably restrict the applicability of slender structures, especially under the influence of temperature. With the aim of achieving reliable prediction of temperature-driven failures in thin-walled structures, this research is concerned with the development of a thermodynamically consistent framework for the coupled thermo-mechanical phase-field model for thin-walled structures using a fully-integrated finite elements. This enables the use of three-dimensional constitutive thermo-mechanical models for the materials. The proposed thermo-mechanical phase-field models are equipped with the Enhanced Assumed Strain (EAS) in order to alleviate Poison and volumetric locking pathologies. This technique is further combined with the Assumed Natural Strain (ANS) method leading to a locking-free thermo-mechanical solid shell phase-field element. A special attention is also paid to evaluation of the corresponding thermodynamic consistency and the variational formalism leading to the non-linear coupled equations equipped with the coupled driving force. Moreover, the same degradation function is used for both displacement field and thermal field. The coupled equations are numerically solved with ad hoc efficient solution schemes for nonlinear problems. Several numerical examples (straight and curved shells) are provided to show the practicality and reliability of the proposed modeling framework. Representative examples assess stable and unstable crack propagation along with their thermo-mechanical interactions.

Keywords: A. Solid Shell, B. Phase-Field fracture, C. Finite Element Method, D: Non-linear Thermo-Elasticity, E. Large Deformations.

1. Introduction

Thermal interactions and the load-bearing capacity of are key aspects to regulate the design, analysis, and production of thin-walled structures. Due to the complex interactions and geometrical definition, the use of analytical methods is rather limited. Therefore, numerical methods lead to a more broad and versatile range of analysis.

The literature regarding the computational procedures for triggering fracture in shell structures can be broadly classifies into 4 categories: (a) Non propagating crack approaches based on the partition of unity methods [1], (b) discrete crack methods such as XFEM [2–5], phantom node models [6], meshless methods [7, 8]. These are largely based on classical shell theories such as Kirchhoff-Love [9–12] (3 parameters), Reissner-Mindlin (5-parameters) [2, 4] and geometrically nonlinear continuum shell [13] for their kinematic description. (c) Cohesive zone models [14–17] implemented via interface or contact elements. The above

---

*Corresponding authors
Email address:* `jreinoso@us.es` (J. Reinoso)

mentioned methods require ad-hoc criteria for their initiation and propagation of the crack, and often it is necessary to know the crack path a priori. (d) Continuum-based methods such as non-local or gradient enhanced damage approaches [18–21], which use constitutive equations at the material point level describing damage in the bulk. In contrast to the above mentioned approach, the phase-field approach has emerged as an alternative modeling tool for its ability to describe initiation, propagation, and handle complex crack paths through the minimization of the total energy (elastic and dissipative due to cracks) of the system, see [22–26] and the references therein. Isogeometric shell analysis could be used as notable alternative modelling tool largely developed [27–29] for the analysis of shells and integrate CAD with CAE.

In this context, the phase-field (PF) approach to fracture originally proposed by Francfort and Marigo [30] and subsequently developed in [31] is very promising. The PF method approximates the original theory developed by Griffith and Irwin as a free discontinuity problem [32] using a diffusive representation of the crack by introducing an internal length scale l for nonlocal damage evolution. It postulates that the crack propagation is due to competition between the strain energy created in the bulk and the surface energy/crack energy related to the creation of new crack paths/surfaces. This further leads to a minimization problem whose solution is sought using variational formulations, see [31] for more details, and [33] for a detailed review of the phase-field approach. The PF approach of fracture has been applied to different applications such as brittle materials [31], ductile fracture [34–36], composites [37–43], heterogeneous media [40], hydrogen assisted cracking in metals [44], functionally graded materials [45, 46], solid shell structures [22–25, 47] to name a few. Thermo-mechanics with phase-field has been developed in recent years, see [36] and the references therein.

Regarding the thermo-mechanical coupling, recently, R. G. Tangella et al [48] proposed the hybrid phase-field model to predict complex crack paths in quasi-static thermo-elastic brittle fracture. H. Badnava et al [49] suggested an h-adaptive thermo-mechanical phase-field model, T.-T. Nguyen et al [50] postulated the chemo-thermo-mechanical coupling for the phase-field to predict early age shrinkage in cement-based materials, whereas A. Dean at al [36, 51] proposed invariant-based anisotropic material models for short fiber-reinforced thermoplastics, to name a few of recent contributions. On the other hand, W. Shu et al [52] proposed a thermo-mechanical solid shell for reduced integration and with the Enhanced Assumed Strain (EAS) and Assumed Natural Strain (ANS) methods to avoid hourglass locking [52], and P.K.Asur Vijaya Kumar et al [26] proposed a thermo-mechanical solid shell formulation for geometric non-linearity having full integration, incorporating EAS and ANS methods to alleviate the locking pathologies. However, at present, the application of the PF approach of fracture to thermo-mechanical analysis of thin-walled structures relying on the solid shell concept is largely unexplored.

This work presents phase-field modeling of fracture fully coupled with thermo-mechanics for the failure analysis of thin-walled structures using the solid shell concept. In order to avoid the complex update of rotational tensor, the shell model presented exploits the solid shell concept aforementioned which parametrizes the top and bottom surface of the body [53–57], see [58–62] for alternative formulations. By the virtue of this kinematic description, the solid shell approach features a discretization identical to that of 8 node brick element [54, 63, 64]. Within this framework, three-dimensional constitutive equations (such as) thermo-elastic Kirchhoff-Saint-Venant Material Model is considered and extended to accommodate phase-field degradation. Moreover, the elastic energy and the thermal energy are degraded using the same phase-field degradation function. The potential locking pathologies arising due to the intrinsic nature of a shell complying with lower-order kinematic displacement interpolation schemes is alleviated by the combination of the popular Enhanced Assumed Strain (EAS) [61, 65–68] and the Assumed Natural Strain (ANS) [69, 70] methods, in line with the advanced shell formulations discussed in [71–74]. Hence, the volumetric and the Poisson's thickness locking effects are alleviated by EAS, whereas trapezoidal and transverse shear locking are alleviated using the ANS method. Furthermore, a fully coupled scheme between the phase-field and the mixed finite element formulation (particularly EAS) is accordingly condensed using static condensation of the enhancing strain at the element level [67] such that the original coupling is fully preserved.

The article is organized as follows. Section 2 outlines the principle aspects of the solid shell, thermo-mechanical couplings, and the corresponding constitutive equations. Section 3 presents the variational formulation of the finite element formulation as a minimization problem, finite element approximation of the problem, along with the linearization principles leading to a system of linear equations. In this regard,
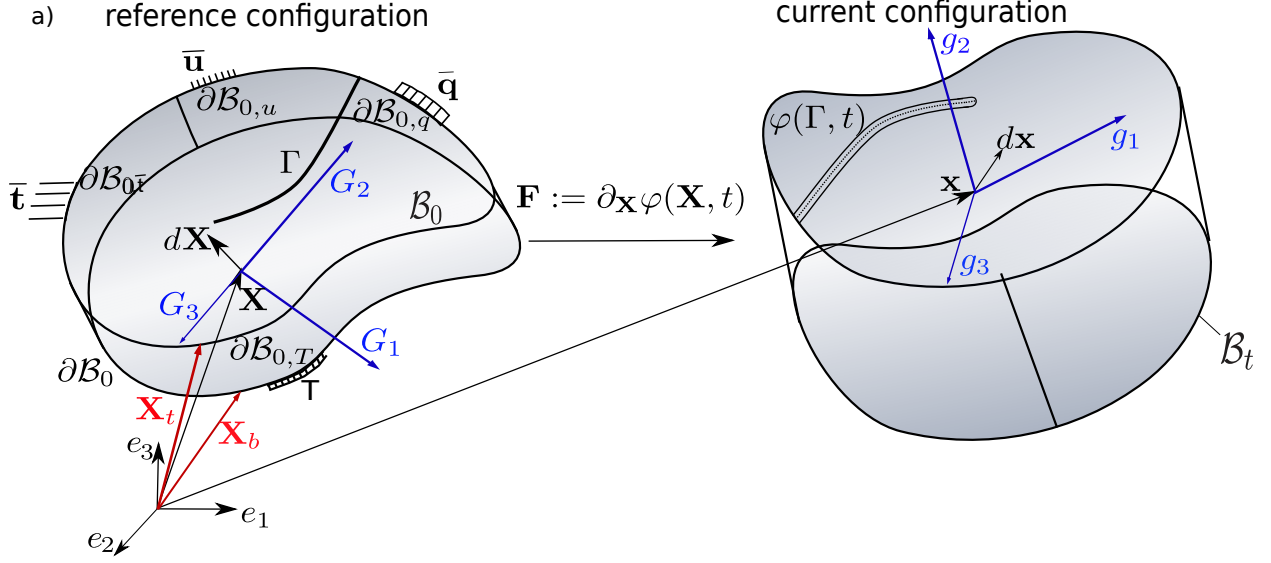
Figure 1: Finite deformation of a body: reference and current configurations. Deformation mapping $\boldsymbol{\varphi}(\mathbf{X}, t)$, that transforms at time t the reference configuration $\mathcal{B}_0$ onto the current configuration $\mathcal{B}_t$, and the displacement-derived deformation gradient $\mathbf{F}^u := \partial_{\mathbf{X}} \boldsymbol{\varphi}(\mathbf{X}, t)$.

the Hu-Washizu principle is adopted for removing the locking pathologies through EAS, and ANS methods. Section 4 presents the numerical examples concerning the phase-field approximation thermo-mechanical solid shell is presented with several benchmark examples, and the role of temperature in each example is pointed out. Finally, the main conclusions of the work is drawn in Section 5.

2. Coupled thermo-mechanical formulation

The initial boundary value problem (IBVP) for coupled thermo-mechanical solid shell with phase-field damage is characterised by: (i) the deformation field of the solid shell, (ii) the temperature field, and (iii) the scalar valued phase-field variable. In the sequel, the basic aspects and definitions are introduced for the sake of clarity.

2.1. Primary fields of thermo-mechanical analysis

Let $\mathcal{B}_0 \subset \mathbb{R}^{n_{dim}}$ denote a reference configuration of a continuum body in n_{dim} Euclidean space with its delimiting boundary $\partial \mathcal{B}_0 \subset \mathbb{R}^{n_{dim}-1}$. For every position vector $\mathbf{X} \in \mathcal{B}_0$, define the vector valued displacement field $\mathbf{u}(\mathbf{X}, t) : \mathcal{B}_0 \times [0, t] \to \mathbb{R}^3$, the smooth scalar valued temperature $T(\mathbf{X}, t) : \mathcal{B}_0 \times [0, t] \to \mathbb{R}_+$, and a smooth scalar valued function of damage (phase-field) $\mathfrak{d}(\mathbf{X}, t) : \mathcal{B}_0 \times [0, t] \to [0, 1]$, for time interval $[0, t]$, here $\mathfrak{d} = 0$ refers to intact material and $\mathfrak{d} = 1$ refers to a cracked material.

The fields in the reference configurations are assumed to be a consequence of prescribed: (i) displacement $\mathbf{u} = \bar{\mathbf{u}}$ on $\partial \mathcal{B}_{0,u}$, (ii) traction $\bar{\mathbf{t}} = \boldsymbol{\sigma} \cdot \mathbf{n}(\mathbf{X}, t)$ on $\partial \mathcal{B}_{0,\bar{t}}$ for the Cauchy stress $\boldsymbol{\sigma}$ and outwards normal $\mathbf{n}$, (iii) temperature T_0 on $\partial \mathcal{B}_{0,T}$, and (iv) heat flux $\boldsymbol{Q}_N$ on $\partial \mathcal{B}_{0,q}$ such that $\partial \mathcal{B}_0 = \overline{\partial \mathcal{B}_{0,u} \cup \partial \mathcal{B}_{0,\bar{t}} \cup \partial \mathcal{B}_{0,T} \cup \partial \mathcal{B}_{0,q}}$ and $\partial \mathcal{B}_{0,u} \cap \partial \mathcal{B}_{0,\bar{t}} = \emptyset$, $\partial \mathcal{B}_{0,T} \cap \partial \mathcal{B}_{0,q} = \emptyset$ as in Fig. 1.

Define a single valued continuously differentiable function $\boldsymbol{\varphi}(\mathbf{X}, t) : \mathcal{B}_0 \times [0, t] \to \mathbb{R}^3$ that maps the reference material point $\mathbf{X} \in \mathcal{B}_0$ onto the current configuration point $\mathbf{x} \in \mathcal{B}_t$, such that $\mathbf{x} = \boldsymbol{\varphi}(\mathbf{X}, t) = \mathbf{X} + \mathbf{u}(\mathbf{X}, t)$ for each t. The operator $\boldsymbol{\varphi}(\mathbf{X}, t)$ is then subjected to local conditions

$$\mathbf{F}^u := \partial_{\mathbf{X}} \boldsymbol{\varphi}(\mathbf{X}, t) = \nabla_{\mathbf{X}} \boldsymbol{\varphi}(\mathbf{X}, t) = 1 + \nabla \mathbf{u} = \frac{\partial \mathbf{x}}{\partial \mathbf{X}} \in \mathbb{R}^{n_{dim} \times n_{dim}}, \quad \text{and} \quad J^u := \det[\mathbf{F}^u] > 0.$$

3

Here, $\mathbf{F}^u$, J^u and $\nabla\mathbf{u}$ are displacement-derived deformation gradient, the Jacobian operator, and the displacement gradient, respectively, where $\det[\bullet]$ stands for the determinant operator.

Note that the operator $\mathbf{F}^u$ represents a linear map between the unit reference element $\mathrm{d}\mathbf{X}$ onto the current element $\mathrm{d}\mathbf{x}$. The co-variant basis as in Fig. 1 in reference $(\mathbf{G}_i)$ and the current configurations $(\mathbf{g}_i)$ are defined as

$$\mathbf{G_i}(\xi) := \frac{\partial \mathbf{X}(\xi)}{\partial \xi^i}, \quad \mathbf{g_i}(\xi) := \frac{\partial \mathbf{x}(\xi)}{\partial \xi^i}, \qquad i = \{1,2,3\}. \tag{1}$$

The metric tensors now take the form $\mathbf{G} = G_{ij}\mathbf{G}^i \otimes \mathbf{G}^j = G^{ij}\mathbf{G}_i \otimes \mathbf{G}_j$ in the reference configuration and $\mathbf{g} = g_{ij}\mathbf{g}^i \otimes \mathbf{g}^j = g^{ij}\mathbf{g}_i \otimes \mathbf{g}_j$ in the current configuration. Here, $\mathbf{G}^i$ and $\mathbf{g}^i$ are contravariant basis in reference and current configuration satisfying the standard relationship $\mathbf{G}_i.\mathbf{G}^j = \delta_i^j$ and $\mathbf{g}_i.\mathbf{g}^j = \delta_i^j$. The displacement-derived deformation gradient $\mathbf{F}^u$ in the curvilinear setting reads

$$\mathbf{F}^u := \mathbf{g}_i \otimes \mathbf{G}^i. \tag{2}$$

Furthermore, the displacement-derived left $\mathbf{C}^u$ Cauchy-Green deformation tensor takes the form

$$\mathbf{C}^u := [\mathbf{F}^u]^{\mathrm{T}} \cdot \mathbf{g} \cdot [\mathbf{F}^u] = g_{ij}\mathbf{G}^i \otimes \mathbf{G}^j, \tag{3}$$

whereas the displacement-derived Green-Lagrangian strain tensor takes the form

$$\mathbf{E}^u := \frac{1}{2}\left[\mathbf{C}^u - \mathbf{G}\right] = \frac{1}{2}\left[g_{ij} - G_{ij}\right]\mathbf{G}^i \otimes \mathbf{G}^j. \tag{4}$$

The displacement-derived Green-Lagrangian strain tensor is enhanced by the considering incompatible Green-Lagrangian tensor $\tilde{\mathbf{E}}$ in order to avoid locking pathologies. This is achieved by additive decomposition of the total Green-Lagrangian strain tensor which constitutes the central idea of EAS, in line with [61], as

$$\mathbf{E} := \mathbf{E}^u + \tilde{\mathbf{E}}. \tag{5}$$

Consequently, the enhanced right Cauchy-Green tensor $\mathbf{C}$ is modified to accommodate the total Green-Lagrangian strain tensor and it takes the form

$$\mathbf{C} := \mathbf{C}^u + \tilde{\mathbf{C}} = 2(\mathbf{E}^u + \tilde{\mathbf{E}}) + \mathbf{G}. \tag{6}$$

In order to compute the enhanced right Cauchy-Green tensor, the displacement-derived deformation field can be decomposed into the rotation tensor $\mathbf{R}$ and the compatible right stretch tensor $\mathbf{U}^u$ as $\mathbf{F}^u = \mathbf{R}\mathbf{U}^u$ by applying the polar decomposition theorem. The modified right stretch tensor $\mathbf{U}$ is then estimated via Eq. (6) accounting for the enhanced strains, and it takes the form $\mathbf{U} := \mathbf{C}^{\frac{1}{2}}$. With this, the modified deformation gradient yields

$$\mathbf{F} := \mathbf{R} \cdot \mathbf{U}, \tag{7}$$

with $J = \det[\mathbf{F}]$ being the corresponding modified Jacobian.

The second Piola-Kirchhoff stress tensor $\mathbf{S}$ (referred as PK2 in the related literature) in the reference configuration is estimated using the Cauchy stress tensor as

$$\mathbf{S} = \mathbf{F}^{-1} \cdot \mathbf{P} = J\mathbf{F}^{-1} \cdot \boldsymbol{\sigma} \cdot \mathbf{F}^{-1} = S^{ij}\mathbf{G}_i \otimes \mathbf{G}_j, \tag{8}$$

4

where S^{ij} identifies its contravariant component.

Analogous to the stress tensor, the heat flux vector $\mathbf{Q}$ can be obtained in the reference configuration using the Cauchy heat flux $\mathbf{q}$ in the current configuration as

$$\mathbf{Q} = \mathrm{J}\mathbf{F}^{-1} \cdot \mathbf{q} = Q^i \mathbf{G}_i, \tag{9}$$

where, Q^i identifies its contravariant component.

2.2. Global equations of thermo-elasticity

The constitutive equations are derived such that they comply with the essential balance principle (conservation law) and second law of thermodynamics, which in its local material version is identified as the Clausius-Duhem inequality. Assuming a local theory, the constitutive law postulates that the Helmholtz free energy function Ψ depends on the modified Green-Lagrangian strain tensor $\mathbf{E}$, the temperature T and its spacial gradient $\nabla_{\mathbf{X}} T$, phase-field (excluded here) and a set of internal variables $\boldsymbol{\mathcal{I}}$ as

$$\rho_0 \Psi = \hat{\Psi}(\mathbf{E}, T, \nabla_{\mathbf{X}} T, \boldsymbol{\mathcal{I}}), \tag{10}$$

for ρ_0 being the material density in reference configuration. For the isotropic Kirchhoff-Saint-Venant material model, the Helmholtz free energy reads

$$\Psi(\mathbf{E}, T) = \quad \tfrac{1}{2}\lambda \left(\mathrm{tr}[\mathbf{E}]\right)^2 + \mu \mathrm{tr}[\mathbf{E}^2] - 3\kappa\alpha\mathrm{tr}[\mathbf{E}]\left(T - T_0\right) \quad + c_p \left[\left(T - T_0\right) - T \log \frac{T}{T_0}\right], \tag{11}$$

where λ and μ are the Lamé constants, κ identifies the bulk modulus, and α is the coefficient of thermal expansion and T_0 is the initial reference temperature.

As mentioned earlier, the constitutive law follows the energy balance with respect to the reference configuration as

$$\begin{cases} \rho_0 = \mathrm{J}\rho : & \text{Local mass balance} \\ \rho_0 \ddot{\boldsymbol{\varphi}} = \mathrm{DIV}\left[\mathbf{P}\right] + \rho_0 \bar{\boldsymbol{\gamma}} = \mathbf{0} : & \text{Linear Momentum balance} \\ \rho_0 \dot{e} = \mathbf{S} : \dot{\mathbf{E}} + R - \mathrm{DIV}\left[\mathbf{Q}\right] : & \text{Energy balance} \end{cases} \tag{12}$$

Here, $\rho_0(\mathbf{X})$ and $\rho(\mathbf{X}, t)$ are the density fields in the reference and current configurations, respectively. Whilst, $\rho_0 \bar{\boldsymbol{\gamma}}$ identifies the prescribed body forces per unit of reference volume, e stands for the specific internal energy whose temporal rate given by $\dot{e}$, $\dot{\mathbf{E}}$ represents the rate of Green-Lagrange strain tensor, R is the internal heat source measured per unit reference volume.

The second law of thermodynamics which ensures the consistency of the formulation takes the form

$$\mathcal{D} = \mathcal{D}_{\mathrm{loc}} + \mathcal{D}_{\mathrm{cond}} = \left[\mathbf{S} : \dot{\mathbf{E}} - \rho_0 \left(\dot{\Psi} + \dot{T}\eta\right)\right] - \left[\frac{1}{T}\mathbf{Q} \cdot \nabla_{\mathbf{X}} T\right] \geq 0, \tag{13}$$

which is referred as Clausius-Duhem inequality, with $\mathcal{D}$ representing the dissipated energy, $\mathcal{D}_{\mathrm{loc}}$ the energy due to the local actions and $\mathcal{D}_{\mathrm{cond}}$ is the energy due to heat conduction. It is easy to see that by enforcing

$$\mathcal{D}_{\mathrm{loc}} \geq 0, \quad \text{and} \quad \mathcal{D}_{\mathrm{cond}} \geq 0, \tag{14}$$

the Clausius-Duhem inequality in Eq. (13) is satisfied, leaving Clausius-Planck inequality Eq. $(14)_1$ and the Fourier inequality $(14)_2$.

Inserting the free energy function in Eq. (10), and Eq. (11) into Eq. (13) satisfies the Clausius-Duhem inequality by following the Coleman and Noll procedure [75] with

$$\mathcal{D}_{\mathrm{loc}} = [\mathbf{S} - \partial_{\mathbf{E}}\Psi] : \dot{\mathbf{E}} - [\eta + \partial_T \Psi]\dot{T} - \partial_{\nabla_{\mathbf{X}}T}\Psi : \nabla_{\mathbf{X}}\dot{T} - \partial_{\mathcal{I}}\Psi : \dot{\mathcal{I}} \geq 0, \tag{15}$$

Accordingly, the constitutive equations corresponding to the second Piola-Kirchhoff tensor, and entropy reads

$$\mathbf{S} := \partial_{\mathbf{E}}\Psi = \lambda\left(\mathrm{tr}[\mathbf{E}]\right)\mathbf{1} + 2\mu\mathbf{E} - 3\kappa\alpha\left(T - T_0\right)\mathbf{1}, \tag{16}$$

$$\eta := -\partial_T\Psi = 3\kappa\alpha\mathrm{tr}[\mathbf{E}] + c_p\log\frac{T}{T_0}, \tag{17}$$

Consequently, the internal dissipation reads

$$\mathcal{D}_{\mathrm{loc}} := -\partial_{\mathcal{I}}\Psi : \dot{\mathcal{I}} \geq 0, \tag{18}$$

accouting for the evolution of inelastic processes such as visco-elastic, plastic effects, among others. Note that damage variable can be added here to the local action $\mathcal{D}_{\mathrm{loc}}$ as $\partial_{\mathfrak{d}}\Psi : \dot{\mathfrak{d}}$, the irreversibility condition and Karush-Kuhn-Tucker (KKT) conditions can be readily obtained as a consequence of Eq.(18) and Eq.(15). In order to keep the formulation close to the original phase-field formulation as in [31] i.e as a competition between the elastic (thermo-elastic) and the surface energy/crack energy, the phase-field variable is added at a later stage as in Section 3.

Based on the Legendre transformation, the evolution equation for entropy η takes the form

$$\rho_0\dot{\eta}T = -\partial_{\mathcal{I}}\Psi : \dot{\mathcal{I}} + R - \mathrm{DIV}[\mathbf{Q}] = \mathcal{D}_{\mathrm{loc}} + R - \mathrm{DIV}[\mathbf{Q}]. \tag{19}$$

The left hand side of Eq.(19) can be expressed as:

$$\rho_0\eta\dot{T} = c_p\dot{T} - \rho_0\mathcal{H}, \tag{20}$$

where the heat capacity, c_p, and the structural heating $\mathcal{S}_H$ due to the rate of temperature reads

$$c_p := -\rho_0 T \partial_{TT}^2 \Psi; \tag{21}$$

$$\mathcal{S}_H := T\partial_{T\mathbf{E}}^2\Psi : \dot{\mathbf{E}} + T\partial_{T\mathcal{I}}^2\Psi : \dot{\mathcal{I}} = T\mathbf{Z} : \dot{\mathbf{E}} + T\mathcal{Q} : \dot{\mathcal{I}},$$

where $\mathbf{Z}$ is the second order tensor containing the thermal conductivity $\mathbf{k}$ in the curvilinear setting associated with the Helmholtz free energy, and $\mathcal{Q}$ identifies the internal variable operator. For an adiabatic process, $\mathrm{DIV}[\mathbf{Q}] \equiv 0$ and $R \equiv 0$. Since there is no irreversible evolution in interval variables (phase-field not included yet), $\partial_{T\mathcal{I}}^2\Psi = 0$ in above equation and hereafter.

The constitutive operators in the curvilinear setting reads

$$\mathbb{C} = \partial_{\mathbf{EE}}\Psi = \left[\lambda G^{ij}G^{kl} + \mu\left(G^{ik}G^{jl} + G^{il}G^{jk}\right)\right]\mathbf{G}_i \otimes \mathbf{G}_j \otimes \mathbf{G}_k \otimes \mathbf{G}_l,$$
$$\mathbf{Z} = -3\kappa\alpha\left[G^{ij}\mathbf{G}_i \otimes \mathbf{G}_j\right], \tag{22}$$

$$\mathbf{Q} = -J\mathbf{F}^{-1} \cdot \mathbf{k} \cdot \mathbf{F}^{-\mathrm{T}} \cdot \nabla_{\mathbf{X}}T = -Jk\left(\mathbf{G}_i \otimes \mathbf{g}^i\right)\left(g^{kl}\mathbf{g}_k \otimes \mathbf{g}_l\right)\left(\mathbf{g}^j \otimes \mathbf{G}_j\right)\nabla_{\mathbf{X}}T = -Jk\mathbf{C}^{-1} \cdot \nabla_{\mathbf{X}}T. \tag{23}$$

Here, the isotropic conductivity is written using the contravariant basis vector as $\mathbf{k} = kg^{ij}\mathbf{g}_i \otimes \mathbf{g}_i$, and $\mathbf{C}^{-1}$ stands for the inverse of the right Cauchy-Green strain tensor. By assuming a isotropic heat flux in the reference configuration, the formulation for the heat flux can be further simplified to $\mathbf{Q} = -k_0\mathbf{G} \cdot \nabla_{\mathbf{X}}T$, where k_0 identifies the thermal conductivity in the reference configuration.

3. Variational basis and finite element formulation

Based on the previous considerations, and assuming a scalar isotropic degradation of the Helmholtz free energy function in Eq.(11) due to the evolution of fracture, the variational basis for the thermo-mechanical phase-field problem is herewith described. Within the framework of Hu-Washizu variational principle, the modified version of the Helmholtz free energy function incorporating the EAS method and the surface energy created due to fracture takes the form

$$\Pi(\mathbf{u}, \tilde{\mathbf{E}}, \mathfrak{d}, T) = \int_{\mathcal{B}_0} g(\mathfrak{d})\Psi(\mathbf{u}, \tilde{\mathbf{E}}, T)\mathrm{d}\Omega - \int_{\mathcal{B}_0} \mathbf{S} : \tilde{\mathbf{E}} \ \mathrm{d}\Omega + \int_{\mathcal{B}_0} \frac{G_C}{2}\left[\frac{\alpha(\mathfrak{d})}{l} + l\left|\nabla\mathfrak{d}\right|^2\right] \ \mathrm{d}\Omega + \Pi_{\mathrm{ext}}. \tag{24}$$

Here, $\alpha(\mathfrak{d}) := \mathfrak{d}^2$ is a continuous monotonic function with $\alpha(0) = 0$ and $\alpha(1) = 1$, called the geometric crack function [45, 76–78]. The term $\frac{\alpha(\mathfrak{d})}{l}$ refers to the local part of the crack surface and $l\left|\nabla\mathfrak{d}\right|^2$ is the non local part. Moreover, $g(\mathfrak{d}) := [(1 - \mathfrak{d})^2 + \mathfrak{x}_k]$ refers to the energetic degradation function that is used to deteriorate the initial coupled thermo-mechanical Helmholtz free energy function with $g(\mathfrak{d}) : [0, 1] \to [1, 0]$ and $\mathfrak{x}_k$ refers to a residual stiffness.

Recalling the additive decomposition of the strain field in Eq. (5), it is important to note that the orthogonality condition between the interpolation spaces of the stress and enhanced strain fields can be exploited from the subsequent derivations.

With this at hand, the solution of Eq.(24) can be obtained by solving it as a minimization problem

$$\boxed{\begin{aligned} &\text{Determine} \quad (\mathbf{u}, \tilde{\mathbf{E}}, \mathfrak{d}, T) \quad \text{from} \\ &(\mathbf{u}^*, \tilde{\mathbf{E}}^*, \mathfrak{d}^*, T^*) = \arg\min_{\mathcal{S}} \Pi(\mathbf{u}, \tilde{\mathbf{E}}, \mathfrak{d}, T), \end{aligned}} \tag{25}$$

with $\mathcal{S} = \{\dot{\mathfrak{d}} \geq 0 \text{ for all } \mathbf{x} \in \mathcal{B}_0\}$. The quadruplet set $(\mathbf{u}^*, \tilde{\mathbf{E}}^*, \mathfrak{d}^*, T^*)$ in Eq. (25) is solved by taking a first variation of the total modified potential functional assuming enough regularity of the fields involved. Recalling the irrivisibility of the damage variables $\mathfrak{d}$, for any admissible test function $(\delta\mathbf{u}, \delta\tilde{\mathbf{E}}, \delta\mathfrak{d}, \delta T)$ in the appropriate space of distribution (see below for details), this leads to the following residual of continuous multi-field problem:

$$\mathcal{R}^u(\mathbf{u}, \tilde{\mathbf{E}}, \mathfrak{d}, T, \delta\mathbf{u}) = \int_{\mathcal{B}_0} g(\mathfrak{d})\left[\mathbf{S} : \delta\mathbf{E}^u\right] \ \mathrm{d}\Omega - \int_{\mathcal{B}_0} \rho_0\bar{\gamma}\delta\mathbf{u} \ \mathrm{d}\Omega - \int_{\partial\mathcal{B}_{0,t}} \hat{\mathbf{t}} \cdot \delta\mathbf{u} \ \mathrm{d}\partial\Omega = 0, \tag{26}$$
$$\mathcal{R}^u = \mathcal{R}^u_{\mathrm{int}} - \mathcal{R}^u_{\mathrm{ext}} = 0,$$

for all $\delta\mathbf{u} \in \mathfrak{B}^u$ with $\mathfrak{B}^u = \{\delta\mathbf{u} \in \mathbf{H}^1(\mathcal{B}_0), \delta\mathbf{u} = 0 \text{ on } \partial\mathcal{B}_{0,\mathbf{u}}\}$. Here, $\rho_0\bar{\gamma}$ denotes the external force applied per unit volume. The residual vector associated with the incompatible strain tensor takes the form

$$\mathcal{R}^{\tilde{E}}(\mathbf{u}, \tilde{\mathbf{E}}, \mathfrak{d}, T, \delta\tilde{\mathbf{E}}) = \int_{\mathcal{B}_0} g(\mathfrak{d})\left[\mathbf{S} : \delta\tilde{\mathbf{E}}\right] \ \mathrm{d}\Omega = \mathcal{R}^{\tilde{E}}_{\mathrm{int}} = 0, \tag{27}$$

for all $\delta\tilde{E} \in \mathfrak{B}^{\tilde{E}}$ with $\mathfrak{B}^{\tilde{E}} = \{\delta\tilde{E} \in \mathbf{L}^2(\mathcal{B}_0)\}$. The residual associated with the phase-field variable takes the form

$$\mathcal{R}^{\mathfrak{d}}(\mathbf{u}, \tilde{\mathbf{E}}, \mathfrak{d}, T, \delta\mathfrak{d}) = \int_{\mathcal{B}_0} G_C\left[\frac{\mathfrak{d}}{l}\delta\mathfrak{d} + l\nabla\mathfrak{d} \cdot \nabla\delta\mathfrak{d}\right] \ \mathrm{d}\Omega - \int_{\mathcal{B}_0} 2(1 - \mathfrak{d})\Psi(\mathbf{u}, \tilde{\mathbf{E}}, T)\delta\mathfrak{d} \ \mathrm{d}\Omega = 0, \tag{28}$$

for all $\delta\mathfrak{d} \in \mathfrak{B}^{\mathfrak{d}}$ with $\mathfrak{B}^{\mathfrak{d}} = \{\delta\mathfrak{d} \in H^1(\Omega)\big|\delta\mathfrak{d} \geq 0 \ \forall \ \mathbf{X} \in \mathcal{B}_0\}$. In the absence of other dissipative mechanisms and heat source ($R \equiv 0$), the residual for the coupled thermal field reads

$$\mathcal{R}^T(\mathbf{u}, \tilde{\mathbf{E}}, \mathfrak{d}, T, \delta T) = \int_{\mathcal{B}_0} c_p\dot{T}\delta T \ \mathrm{d}\Omega - \int_{\mathcal{B}_0} g(\mathfrak{d})\left[T\mathbf{Z} : \dot{\mathbf{E}}\right]\delta T \ \mathrm{d}\Omega + \int_{\mathcal{B}_0} \mathrm{DIV}[\mathbf{Q}]\delta T \ \mathrm{d}\Omega = 0, \tag{29}$$

7

for all $\delta T \in \mathfrak{B}^T$ with $\mathfrak{B}^T = \{\delta T \in H^1(\Omega) \big| \delta T = 0 \text{ on } \partial\mathcal{B}_{0,q}\}$. The third term in Eq.(29) can be reformulated using the divergence theorem as

$$\int_{\mathcal{B}_0} \text{DIV}[\mathbf{Q}]\delta T \; \text{d}\Omega = \int_{\partial\mathcal{B}_{0,q}} \boldsymbol{Q}_N \delta T \; \text{d}\partial\Omega - \int_{\mathcal{B}_0} \mathbf{Q} \cdot \nabla_\mathbf{X} \delta T \; \text{d}\Omega, \tag{30}$$

where $Q_N = \mathbf{Q} \cdot \mathbf{N}$ refers to the Neumann boundary condition on $\partial\mathcal{B}_{0,q}$. With this, the variational form of energy balance equation at the reference configuration takes the form

$$\mathcal{R}^T(\mathbf{u}, \tilde{\mathbf{E}}, \mathfrak{d}, T, \delta T) = \int_{\mathcal{B}_0} c_p \dot{T}\delta T \; \text{d}\Omega - \int_{\mathcal{B}_0} g(\mathfrak{d}) \Big[T\mathbf{Z} : \dot{\mathbf{E}}\Big] \delta T \; \text{d}\Omega + \int_{\partial\mathcal{B}_{0,q}} \boldsymbol{Q}_N \delta T \; \text{d}\partial\Omega - \int_{\mathcal{B}_0} \mathbf{Q} \cdot \nabla_\mathbf{X} \delta T \; \text{d}\Omega = 0. \tag{31}$$

Through the insertion of the Duhamel's law, Eq.(23)$_1$

$$\mathcal{R}^T(\mathbf{u}, \tilde{\mathbf{E}}, \mathfrak{d}, T, \delta T) = \int_{\mathcal{B}_0} c_p \dot{T}\delta T \; \text{d}\Omega - \int_{\mathcal{B}_0} g(\mathfrak{d}) \Big[T\mathbf{Z} : \dot{\mathbf{E}}\Big] \delta T \; \text{d}\Omega + \int_{\partial\mathcal{B}_{0,q}} \boldsymbol{Q}_N \delta T \; \text{d}\partial\Omega$$
$$+ \int_{\mathcal{B}_0} [\nabla_\mathbf{X}\delta T]^\text{T} \cdot J\mathbf{F}^{-1} \cdot \mathbf{k} \cdot \mathbf{F}^{-\text{T}} \cdot \nabla_\mathbf{X} T \; \text{d}\Omega = 0. \tag{32}$$

For isotropic thermal conductivity, Eq.(23)$_2$, the temperature residual finally reads

$$\mathcal{R}^T(\mathbf{u}, \tilde{\mathbf{E}}, \mathfrak{d}, T, \delta T) = \int_{\mathcal{B}_0} c_p \dot{T}\delta T \; \text{d}\Omega - \int_{\mathcal{B}_0} g(\mathfrak{d}) \Big[T\mathbf{Z} : \dot{\mathbf{E}}\Big] \delta T \; \text{d}\Omega$$
$$+ \int_{\partial\mathcal{B}_{0,q}} \boldsymbol{Q}_N \delta T \; \text{d}\partial\Omega + \int_{\mathcal{B}_0} Jk \, [\nabla_\mathbf{X}\delta T]^\text{T} \cdot \mathbf{C}^{-1} \cdot \nabla_\mathbf{X}[T] \; \text{d}\Omega = 0. \tag{33}$$

Notice that, the degradation function $g(\mathfrak{d})$ is added in Eq. (32). Meaning that, the thermal conductivity associated in $\mathbf{Z}$ is degraded. As the phase-field value reaches $\mathfrak{d} = 1$, the thermal conductivity approaches zero acting as a potential barrier for the heat transfer across the cracked region Γ.

3.1. Finite Element Formulation

The finite element discretization is introduced on the reference configuration $\mathcal{B}_0$ following the standard arguments of isoparametric interpolation. The functional space $\mathcal{B}_0$ is discretized into n_e non-overlapping elements, such that $\mathcal{B}_0 \approx \bigcup_{e=1}^{n_e} \mathcal{B}_0^{(e)}$. Complying with the solid shell approach, for the natural coordinate system (ξ^1, ξ^2, ξ^3), the position vector at reference and current configuration $\mathbf{X}$ and $\mathbf{x}$ are expressed by the points of top and bottom surface $\mathbf{X}_t(\xi^1, \xi^2)$ and bottom surfaces $\mathbf{X}_b(\xi^1, \xi^2)$ of the shell as in Fig. 1. Accordingly, the position vector in the reference configuration can be expressed as

$$\mathbf{X}(\boldsymbol{\xi}) = \frac{1}{2}\left(1 + \xi^3\right)\mathbf{X}_t(\xi^1, \xi^2) + \frac{1}{2}\left(1 - \xi^3\right)\mathbf{X}_b(\xi^1, \xi^2), \tag{34}$$

whereas the position in the current configuration takes the form

$$\mathbf{x}(\boldsymbol{\xi}) = \frac{1}{2}\left(1 + \xi^3\right)\mathbf{x}_t(\xi^1, \xi^2) + \frac{1}{2}\left(1 - \xi^3\right)\mathbf{x}_b(\xi^1, \xi^2), \tag{35}$$

with the parametric space defined in natural co-ordinates as $\mathcal{A} := \{\boldsymbol{\xi} = (\xi^1, \xi^2, \xi^3) \in \mathbb{R}^3 \mid -1 \leq \xi^i \leq +1; i = 1, 2, 3\}$, with (ξ^1, ξ^2) being in plane and ξ^3 being thickness direction.

Regarding the phase-field variable embedded in the shell body, the definition of position vector is adopted in the reference and current configuration, a possible anszat yields to a linear interpolation between the top ($\mathfrak{d}_t$) and bottom ($\mathfrak{d}_b$) surfaces of the shell in line with [56], expressed as

$$\mathfrak{d}(\boldsymbol{\xi}) = \frac{1}{2}\left(1 + \xi^3\right)\mathfrak{d}_t(\xi^1, \xi^2) + \frac{1}{2}\left(1 - \xi^3\right)\mathfrak{d}_b(\xi^1, \xi^2). \tag{36}$$

The discrete reference (Lagrangian) and current (Eulerian) nodal position vectors are interpolated through standard trilinear shape functions N^I ($\mathbf{N}(\boldsymbol{\xi})$ in matrix notation) as

$$\mathbf{X} \approx \sum_{I=1}^{n_n} N^I(\boldsymbol{\xi})\mathbf{X}_I = \mathbf{N}(\boldsymbol{\xi})\widetilde{\mathbf{X}} \quad \text{and} \quad \mathbf{x} \approx \sum_{I=1}^{n_n} N^I(\boldsymbol{\xi})\mathbf{x}_I = \mathbf{N}(\boldsymbol{\xi})\widetilde{\mathbf{x}}, \tag{37}$$

with number of nodes $n_n = 8$ whose nodal values are collected into the respective global vectors $\widetilde{\mathbf{X}}$ and $\widetilde{\mathbf{x}}$.

The interpolation of the fields ($\mathbf{u}, \tilde{\mathbf{E}}, \mathfrak{d}, T$), their respective variations ($\delta\mathbf{u}, \delta\tilde{\mathbf{E}}, \delta\mathfrak{d}, \delta T$) and their increments ($\Delta\mathbf{u}, \Delta\tilde{\mathbf{E}}, \Delta\mathfrak{d}, \Delta T$) in compact form reads

$$\mathbf{u} \approx \mathbf{N}(\boldsymbol{\xi})\mathbf{d}; \quad \delta\mathbf{u} \approx \mathbf{N}(\boldsymbol{\xi})\delta\mathbf{d}; \quad \Delta\mathbf{u} \approx \mathbf{N}(\boldsymbol{\xi})\Delta\mathbf{d}, \tag{38}$$

$$\tilde{\mathbf{E}} \approx \mathbf{M}(\boldsymbol{\xi})\boldsymbol{\varsigma}, \quad \delta\tilde{\mathbf{E}} \approx \mathbf{M}(\boldsymbol{\xi})\delta\boldsymbol{\varsigma}, \quad \Delta\tilde{\mathbf{E}} \approx \mathbf{M}(\boldsymbol{\xi})\Delta\boldsymbol{\varsigma}, \tag{39}$$

$$\mathfrak{d} \approx \mathbf{N}(\boldsymbol{\xi})\tilde{\mathfrak{d}}; \quad \delta\mathfrak{d} \approx \mathbf{N}(\boldsymbol{\xi})\delta\tilde{\mathfrak{d}}; \quad \Delta\mathfrak{d} \approx \mathbf{N}(\boldsymbol{\xi})\Delta\tilde{\mathfrak{d}} \tag{40}$$

$$T \approx \hat{\mathbf{N}}(\boldsymbol{\xi})\hat{\boldsymbol{T}}, \delta T \approx \hat{\mathbf{N}}(\boldsymbol{\xi})\delta\hat{\boldsymbol{T}}, \Delta T \approx \hat{\mathbf{N}}(\boldsymbol{\xi})\Delta\hat{\boldsymbol{T}}. \tag{41}$$

Here, the $\mathbf{M}(\boldsymbol{\xi})$ denotes the enhancing interpolation matrix and $\boldsymbol{\varsigma}$ is the vector collecting the EAS parameters. In particular, within the element space $\boldsymbol{\xi} = \{\xi^1, \xi^2, \xi^3\}$, the operator $\mathbf{M}(\boldsymbol{\xi})$ takes for form
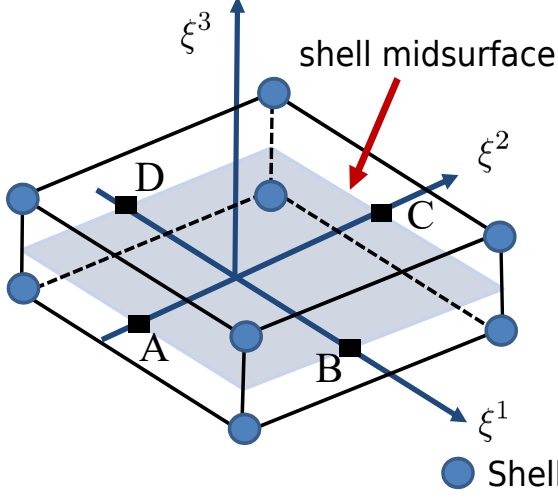
$$\tilde{\mathbf{M}} = \begin{bmatrix} \xi^1 & 0 & 0 & 0 & 0 & 0 & 0 \\ 0 & \xi^1 & 0 & 0 & 0 & 0 & 0 \\ 0 & 0 & \xi^3 & \xi^1\xi^3 & \xi^2\xi^3 & 0 & 0 \\ 0 & 0 & 0 & 0 & 0 & \xi^1 & \xi^2 \\ 0 & 0 & 0 & 0 & 0 & 0 & 0 \\ 0 & 0 & 0 & 0 & 0 & 0 & 0 \end{bmatrix}. \tag{42}$$

The operator $\mathbf{M}(\boldsymbol{\xi})$ with 7 parameter at each element level is suitable to alleviate membrane, volumetric and Poisson's thickness locking pathologies. It is important to note that the interpolation introduced in Eq. (42) should be transformed into the global cartesian space.

In the current solid shell formulation, transverse shear and transverse normal strain components are modified in order to circumvent transverse shear and trapezoidal locking respectively using ANS interpolation method. The interpolation of the transverse shear strains E_{13} and E_{23} are performed at points $\boldsymbol{\xi}_A = (0, -1, 0)$, $\boldsymbol{\xi}_B = (1, 0, 0)$, $\boldsymbol{\xi}_C = (0, 1, 0)$ and $\boldsymbol{\xi}_D = (-1, 0, 0)$ as in Fig. 2. Accordingly, the transverse shear strain components reads

$$\begin{Bmatrix} 2E_{13}^{ANS} \\ 2E_{23}^{ANS} \end{Bmatrix} = \begin{Bmatrix} (1 - \xi^2)2E_{13}(\boldsymbol{\xi}_A) + (1 + \xi^2)2E_{13}(\boldsymbol{\xi}_C) \\ (1 + \xi^1)2E_{23}(\boldsymbol{\xi}_B) + (1 - \xi^1)2E_{23}(\boldsymbol{\xi}_D) \end{Bmatrix}. \tag{43}$$
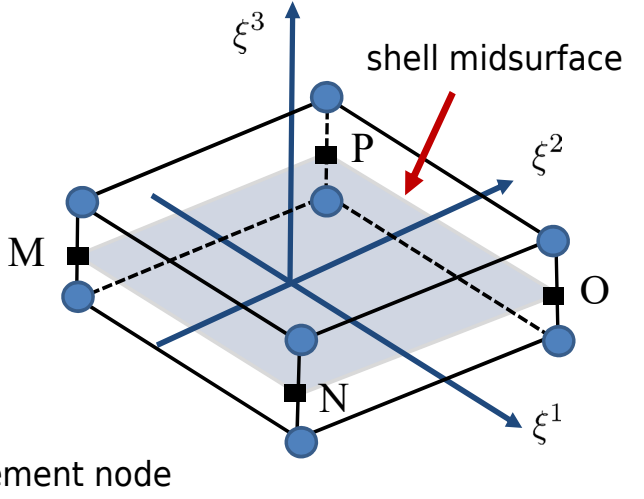
Figure 2: ANS for transverse shear locking and ANS for trapezoidal locking

Similarly, the interpolation of the transverse normal strain E_{33} are performed at points $\boldsymbol{\xi}_O = (-1, -1, 0)$, $\boldsymbol{\xi}_P = (1, -1, 0)$, $\boldsymbol{\xi}_S = (1, 1, 0)$ and $\boldsymbol{\xi}_T = (-1, 1, 0)$ as in Fig. 1. Based on this, the transverse normal strain takes the form

$$
\begin{aligned}
E_{33}^{ANS} &= \sum_{m=M,N,O,P} N^m(\xi^1, \xi^2) E_{33}; \\
N^m(\xi^1, \xi^2) &= \frac{1}{4}\left(1 + \xi_m^1 \xi^1\right)\left(1 + \xi_m^2 \xi^2\right), \\
&\text{with } \xi_m^1, \xi_m^2 = \pm 1.
\end{aligned}
\tag{44}
$$

The interpolation of displacement derived compatible strains are approximated using displacement strain operator $\mathbf{B}$ as

$$
\mathbf{E}^u \approx \mathbf{B(d)d}, \quad \delta\mathbf{E}^u \approx \mathbf{B(d)}\delta\mathbf{d}, \quad \Delta\mathbf{E}^u \approx \mathbf{B(d)}\Delta\mathbf{d}. \tag{45}
$$

Similarly, the gradient of phase-field are interpolated using a suitable operator $\mathbf{B}^\mathfrak{d}$ as

$$
\nabla_{\mathbf{x}}\mathfrak{d} \approx \mathbf{B}^\mathfrak{d}(\mathbf{d})\tilde{\mathfrak{d}}, \quad \nabla_{\mathbf{x}}\delta\mathfrak{d} \approx \mathbf{B}^\mathfrak{d}(\mathbf{d})\delta\tilde{\mathfrak{d}}, \quad \nabla_{\mathbf{x}}\Delta\mathfrak{d} \approx \mathbf{B}^\mathfrak{d}(\mathbf{d})\Delta\tilde{\mathfrak{d}}. \tag{46}
$$

The interpolation of the spatial temperature gradient at current configuration ($\nabla_{\mathbf{X}}T$), and its associated variations can be expressed as

$$
\nabla_{\mathbf{X}}T = \mathbf{G}^{-1}\nabla_{\boldsymbol{\xi}}T \approx \mathbf{G}^{-1}\nabla_{\boldsymbol{\xi}}\hat{\mathbf{N}}(\boldsymbol{\xi})\hat{\boldsymbol{T}}; \quad \nabla_{\mathbf{X}}\delta T \approx \mathbf{G}^{-1}\nabla_{\boldsymbol{\xi}}\hat{\mathbf{N}}(\boldsymbol{\xi})\delta\hat{\boldsymbol{T}}; \quad \nabla_{\mathbf{X}}\Delta T \approx \mathbf{G}^{-1}\nabla_{\boldsymbol{\xi}}\hat{\mathbf{N}}(\boldsymbol{\xi})\Delta\hat{\boldsymbol{T}}, \tag{47}
$$

where $\nabla_{\boldsymbol{\xi}}$ is the gradient of temperature at each node with respect natural coordinate defines in the curvilinear setting.

3.2. Consistent linearization of the coupled thermo-mechanical weak form

Through the insertion of the previously discussed interpolation scheme, the residuals of the independent fields $(\mathbf{u}, \tilde{\mathbf{E}}, \mathfrak{d}, T)$ in the discrete form can be expressed as

$$\hat{\mathcal{R}}_{\text{int}}^{u}(\mathbf{d}, \boldsymbol{\varsigma}, \tilde{\mathfrak{d}}, \hat{\boldsymbol{T}}, \delta\mathbf{d}) = \delta\mathbf{d}^{\text{T}} \left[\int_{\mathcal{B}_0} g(\mathfrak{d})\mathbf{B}(\mathbf{d})^{\text{T}}\mathbf{S} \ \mathrm{d}\Omega \right], \tag{48}$$

$$\hat{\mathcal{R}}_{\text{int}}^{\tilde{E}}(\mathbf{d}, \boldsymbol{\varsigma}, \tilde{\mathfrak{d}}, \hat{\boldsymbol{T}}, \delta\boldsymbol{\varsigma}) = \delta\boldsymbol{\varsigma}^{\text{T}} \left[\int_{\mathcal{B}_0} g(\mathfrak{d})\mathbf{M}(\boldsymbol{\xi})^{\text{T}}\mathbf{S} \ \mathrm{d}\Omega \right], \tag{49}$$

$$\hat{\mathcal{R}}^{\mathfrak{d}}(\mathbf{d}, \boldsymbol{\varsigma}, \tilde{\mathfrak{d}}, \hat{\boldsymbol{T}}, \delta\mathfrak{d}) = \delta\mathfrak{d}^{\text{T}} \left[\int_{\mathcal{B}_0} G_C \left[\frac{1}{l}\mathbf{N}(\boldsymbol{\xi})^{\text{T}}\mathfrak{d} + l\mathbf{B}^{\mathfrak{d}}(\boldsymbol{\xi})^{\text{T}}\nabla_{\mathbf{x}}\mathfrak{d} \right] \ \mathrm{d}\Omega - \int_{\mathcal{B}_0} 2(1-\mathfrak{d})\mathbf{N}^{\text{T}}(\boldsymbol{\xi})\mathcal{H}\delta\mathfrak{d} \ \mathrm{d}\Omega \right], \quad (50)$$

$$\hat{\mathcal{R}}_{\text{int}}^{T}(\mathbf{d}, \boldsymbol{\varsigma}, \tilde{\mathfrak{d}}\hat{\boldsymbol{T}}, \delta\hat{\boldsymbol{T}}) = \delta\hat{\boldsymbol{T}}^{\text{T}} \left[\int_{\mathcal{B}_0} \hat{\mathbf{N}}(\boldsymbol{\xi})^{\text{T}}c_p\dot{T} \ \mathrm{d}\Omega - \int_{\mathcal{B}_0} g(\mathfrak{d})\hat{\mathbf{N}}(\boldsymbol{\xi})^{\text{T}} \left(\mathbf{Z}^{\text{T}}\dot{\mathbf{E}} \right) T \ \mathrm{d}\Omega + \int_{\mathcal{B}_0} J\mathbf{B}_T^{\text{T}}\mathbf{F}^{-1}\cdot\mathbf{k}\cdot\mathbf{F}^{-\text{T}}\cdot\nabla_{\mathbf{X}}T \ \mathrm{d}\Omega \right]. \tag{51}$$

Here,

$$\mathcal{H} = \max_{\tau \in [0,t]} \left[\Psi(\mathbf{u}, \tilde{\mathbf{E}}, T) \right], \tag{52}$$

is the crack driving force (history variable) as defined in [56] to ensure the irreversibility of the phase-field variable $\mathfrak{d}$ and $\mathbf{B}_T$ defines a suitable operator to compute the gradient of the temperature field.

Due to the existence of non-linearity in the multi-field Eqs.(48)- (51), an incremental iterative quasi Newton-Raphson scheme is adopted (details are omitted for the sake of brevity). This is achieved by linearization of the residual in Eq.(48), (49), (50), (51) using directional Gateaux derivatives [26, 45, 56].

For this, consider a finite time increment $\Delta t := t_{n+1}^{(k)} - t_n > 0$, where the fields $(\mathbf{u}, \tilde{\mathbf{E}}, \mathfrak{d}, T)$ at step t_n is assumed to be known. The temporal variation of the fields are expressed as

$$\dot{\hat{\boldsymbol{T}}} = \frac{\hat{\boldsymbol{T}}_{n+1} - \hat{\boldsymbol{T}}_n}{\Delta t}; \quad \dot{\mathbf{E}} = \frac{\mathbf{E}_{n+1} - \mathbf{E}_n}{\Delta t}; \dot{\mathbf{d}} = \frac{\mathbf{d}_{n+1} - \mathbf{d}_n}{\Delta t}; \dot{\boldsymbol{\varsigma}} = \frac{\boldsymbol{\varsigma}_{n+1} - \boldsymbol{\varsigma}_n}{\Delta t}, \tag{53}$$

constituting a backward Euler scheme.

The independent fields $(\mathbf{u}, \tilde{\mathbf{E}}, \mathfrak{d}, T)$ are computed at current time step t_{n+1} via consistent linearization of the residual functions which can be expressed as

$$\begin{aligned}\hat{L}[\hat{\mathcal{R}}^{u}] &= \hat{\mathcal{R}}^{u}(\mathbf{d}, \boldsymbol{\varsigma}, \tilde{\mathfrak{d}}, \hat{\boldsymbol{T}}, \delta\mathbf{d}) + \Delta\hat{\mathcal{R}}^{u}(\mathbf{d}, \boldsymbol{\varsigma}, \tilde{\mathfrak{d}}, \hat{\boldsymbol{T}}, \delta\mathbf{d}, \Delta\mathbf{d}, \Delta\boldsymbol{\varsigma}, \Delta\tilde{\mathfrak{d}}, \Delta\hat{\boldsymbol{T}}) \\ &= \hat{\mathcal{R}}^{u} + \Delta_{\mathbf{d}}\hat{\mathcal{R}}^{u}\Delta\mathbf{d} + \Delta_{\boldsymbol{\varsigma}}\hat{\mathcal{R}}^{u}\Delta\boldsymbol{\varsigma} + \Delta_{\mathfrak{d}}\hat{\mathcal{R}}^{u}\Delta\tilde{\mathfrak{d}} + \Delta_{T}\hat{\mathcal{R}}^{u}\Delta\hat{\boldsymbol{T}}, \end{aligned} \tag{54}$$

$$\begin{aligned}\hat{L}[\hat{\mathcal{R}}^{\tilde{E}}] &= \hat{\mathcal{R}}^{\tilde{E}}(\mathbf{d}, \boldsymbol{\varsigma}, \tilde{\mathfrak{d}}, \hat{\boldsymbol{T}}, \delta\boldsymbol{\varsigma}) + \Delta\hat{\mathcal{R}}^{\tilde{E}}(\mathbf{d}, \boldsymbol{\varsigma}, \tilde{\mathfrak{d}}, \hat{\boldsymbol{T}}, \delta\mathbf{d}, \Delta\mathbf{d}, \Delta\boldsymbol{\varsigma}, \Delta\tilde{\mathfrak{d}}, \Delta\hat{\boldsymbol{T}}) \\ &= \hat{\mathcal{R}}^{\tilde{E}} + \Delta_{\mathbf{d}}\hat{\mathcal{R}}^{\tilde{E}}\Delta\mathbf{d} + \Delta_{\boldsymbol{\varsigma}}\hat{\mathcal{R}}^{\tilde{E}}\Delta\boldsymbol{\varsigma} + \Delta_{\mathfrak{d}}\hat{\mathcal{R}}^{\tilde{E}}\Delta\tilde{\mathfrak{d}} + \Delta_{T}\hat{\mathcal{R}}^{\tilde{E}}\Delta\hat{\boldsymbol{T}} \end{aligned} \tag{55}$$

$$\begin{aligned}\hat{L}[\hat{\mathcal{R}}^{\tilde{\mathfrak{d}}}] &= \hat{\mathcal{R}}^{\tilde{\mathfrak{d}}}(\mathbf{d}, \boldsymbol{\varsigma}, \tilde{\mathfrak{d}}, \hat{\boldsymbol{T}}, \delta\boldsymbol{\varsigma}) + \Delta\hat{\mathcal{R}}^{\tilde{\mathfrak{d}}}(\mathbf{d}, \boldsymbol{\varsigma}, \tilde{\mathfrak{d}}, \hat{\boldsymbol{T}}, \delta\mathbf{d}, \Delta\mathbf{d}, \Delta\boldsymbol{\varsigma}, \Delta\tilde{\mathfrak{d}}, \Delta\hat{\boldsymbol{T}}) \\ &= \hat{\mathcal{R}}^{\tilde{\mathfrak{d}}} + \Delta_{\mathbf{d}}\hat{\mathcal{R}}^{\tilde{\mathfrak{d}}}\Delta\mathbf{d} + \Delta_{\boldsymbol{\varsigma}}\hat{\mathcal{R}}^{\tilde{\mathfrak{d}}}\Delta\boldsymbol{\varsigma} + \Delta_{\mathfrak{d}}\hat{\mathcal{R}}^{\tilde{\mathfrak{d}}}\Delta\tilde{\mathfrak{d}} + \Delta_{T}\hat{\mathcal{R}}^{\tilde{\mathfrak{d}}}\Delta\hat{\boldsymbol{T}} \end{aligned} \tag{56}$$

11

$$\hat{L}[\hat{\mathcal{R}}^T] = \hat{\mathcal{R}}^T(\mathbf{d}, \varsigma, \tilde{\mathfrak{d}}, \hat{\boldsymbol{T}}, \delta\hat{\boldsymbol{T}}) + \Delta\hat{\mathcal{R}}^T(\mathbf{d}, \varsigma, \tilde{\mathfrak{d}}, \hat{\boldsymbol{T}}, \delta\mathbf{d}, \Delta\mathbf{d}, \Delta\varsigma, \Delta\tilde{\mathfrak{d}}, \Delta\hat{\boldsymbol{T}})$$

$$= \hat{\mathcal{R}}^T + \Delta_{\mathbf{d}}\hat{\mathcal{R}}^T\Delta\mathbf{d} + \Delta_{\varsigma}\hat{\mathcal{R}}^T\Delta\varsigma + \Delta_{\mathfrak{d}}\hat{\mathcal{R}}^T\Delta\tilde{\mathfrak{d}} + \Delta_T\hat{\mathcal{R}}^T\Delta\hat{\boldsymbol{T}} \tag{57}$$

where $\Delta_{\mathfrak{b}}[\mathfrak{a}]$ denotes the tangent matrices calculated as a directional derivative of the residual form $\mathfrak{a}$ with respect to the field $\mathfrak{b}$. In particular $\Delta_{\mathfrak{b}}[\mathfrak{a}] = \mathbf{k}_{\mathfrak{ab}}$ with $\{\mathfrak{a}, \mathfrak{b}\} = \{\mathbf{d}, \varsigma, \tilde{\mathfrak{d}}, \hat{\boldsymbol{T}}\}$. Following the standard finite element procedure, Eq.(54), (55), (56), (57) can be expressed as a system of linear equations as

$$\begin{bmatrix} \mathbf{K_{dd}} & \mathbf{K_{d\varsigma}} & \mathbf{K_{d\tilde{\mathfrak{d}}}} & \mathbf{K_{d}}_T \\ \mathbf{K_{\varsigma d}} & \mathbf{K_{\varsigma\varsigma}} & \mathbf{K_{\varsigma\tilde{\mathfrak{d}}}} & \mathbf{K_{\varsigma}}_T \\ \mathbf{K_{\tilde{\mathfrak{d}}d}} & \mathbf{K_{\tilde{\mathfrak{d}}\varsigma}} & \mathbf{K_{\tilde{\mathfrak{d}}\tilde{\mathfrak{d}}}} & \mathbf{K_{\tilde{\mathfrak{d}}}}_T \\ \mathbf{K}_{T\mathbf{d}} & \mathbf{K}_{T\varsigma} & \mathbf{K}_{T\tilde{\mathfrak{d}}} & \mathbf{K}_{TT} \end{bmatrix} \begin{bmatrix} \Delta\mathbf{d} \\ \Delta\varsigma \\ \Delta\mathfrak{d} \\ \Delta\hat{\boldsymbol{T}} \end{bmatrix} = \begin{bmatrix} \hat{\mathcal{R}}^u_{\text{ext}} \\ \mathbf{0} \\ \mathbf{0} \\ \hat{\mathcal{R}}^T_{\text{ext}} \end{bmatrix} - \begin{bmatrix} \hat{\mathcal{R}}^u_{\text{int}} \\ \hat{\mathcal{R}}^\varsigma_{\text{int}} \\ \hat{\mathcal{R}}^{\tilde{\mathfrak{d}}}_{\text{int}} \\ \hat{\mathcal{R}}^T_{\text{int}} \end{bmatrix}. \tag{58}$$

The different elements of the tangent stiffness matrix takes the form

$$\mathbf{K_{dd}} = \int_{\mathcal{B}_0} g(\mathfrak{d}) \left(\mathbf{B(d)}^{\text{T}}\mathbb{C}\mathbf{B(d)} + \left[\frac{\partial\mathbf{B(d)}}{\partial\mathbf{d}}\right]^{\text{T}}\mathbf{S} \right) \, d\Omega = \mathbf{K_{dd,mat}} + \mathbf{K_{dd,geom}} \tag{59a}$$

$$\mathbf{K_{d\varsigma}} = \int_{\mathcal{B}_0} g(\mathfrak{d})\mathbf{M(\boldsymbol{\xi})}^{\text{T}}\mathbb{C}\mathbf{B(d)} \, d\Omega; \tag{59b}$$

$$\mathbf{K_{d\tilde{\mathfrak{d}}}} = \int_{\mathcal{B}_0} -2(1-\mathfrak{d})\mathbf{B(d)}^{\text{T}}\mathbf{SN(\boldsymbol{\xi})} \, d\Omega, \tag{59c}$$

$$\mathbf{K_{d}}_T = \int_{\mathcal{B}_0} g(\mathfrak{d})\mathbf{B(d)}^{\text{T}}\mathbf{Z}\hat{\mathbf{N}}(\boldsymbol{\xi}) \, d\Omega, \tag{59d}$$

$$\mathbf{K}_{\varsigma u} = \int_{\mathcal{B}_0} g(\mathfrak{d})\mathbf{M(\boldsymbol{\xi})}^{\text{T}}\mathbb{C}\mathbf{B(d)} \, d\Omega; \tag{60a}$$

$$\mathbf{K}_{\varsigma\varsigma} = \int_{\mathcal{B}_0} g(\mathfrak{d})\mathbf{M(\boldsymbol{\xi})}^{\text{T}}\mathbb{C}\mathbf{M(\boldsymbol{\xi})} \, d\Omega, \tag{60b}$$

$$\mathbf{K}_{\varsigma\tilde{\mathfrak{d}}} = \int_{\mathcal{B}_0} -2(1-\mathfrak{d})\mathbf{M(\boldsymbol{\xi})}^{\text{T}}\mathbf{SN(\boldsymbol{\xi})} \, d\Omega; \tag{60c}$$

$$\mathbf{K}_{\varsigma T} = \int_{\mathcal{B}_0} \mathbf{M(\boldsymbol{\xi})}^{\text{T}}\mathbf{Z}\hat{\mathbf{N}}(\boldsymbol{\xi}) \, d\Omega \tag{60d}$$

$$\mathbf{K}_{\tilde{\mathfrak{d}}\mathbf{d}} = \int_{\mathcal{B}_0} -2(1-\mathfrak{d})\mathbf{N(\boldsymbol{\xi})}^{\text{T}}\mathbf{SB(d)} \, d\Omega; \tag{61a}$$

$$\mathbf{K}_{\tilde{\mathfrak{d}}\varsigma} = \int_{\mathcal{B}_0} -2(1-\mathfrak{d})\mathbf{N(\boldsymbol{\xi})}^{\text{T}}\mathbf{SM(\boldsymbol{\xi})} \, d\Omega, \tag{61b}$$

$$\mathbf{K}_{\tilde{\mathfrak{d}}\tilde{\mathfrak{d}}} = \int_{\mathcal{B}_0} \left[2\frac{G_c}{l}\mathcal{H}\right] \mathbf{N(\boldsymbol{\xi})}^{\text{T}}\mathbf{N(\boldsymbol{\xi})} \, d\Omega + \int_{\mathcal{B}_0} 2G_c l\mathbf{B}^{\mathfrak{d}}(\boldsymbol{\xi})^{\text{T}}\mathbf{B}^{\mathfrak{d}}(\boldsymbol{\xi}) \, d\Omega, \tag{61c}$$

$$\mathbf{K}_{\tilde{\mathfrak{d}}T} = \int_{\mathcal{B}_0} -2(1-\mathfrak{d})\mathbf{N(\boldsymbol{\xi})}\mathbf{B}^T(\mathbf{d})\hat{\mathbf{N}}(\boldsymbol{\xi}) \, d\Omega, \tag{61d}$$

$$\mathbf{K}_{T\mathbf{d}} = \int_{\mathcal{B}_0} \Delta_{\mathbf{d}}[J]\mathbf{B}_T^{\mathrm{T}}\mathbf{F}^{-1} \cdot \mathbf{k} \cdot \mathbf{F}^{-\mathrm{T}} \cdot \nabla_{\mathbf{X}}T \ \mathrm{d}\Omega$$
$$+ \int_{\mathcal{B}_0} J\mathbf{B}_T^{\mathrm{T}} \left(\Delta_{\mathbf{d}}[\mathbf{F}^{-1}] \cdot \mathbf{k} \cdot \mathbf{F}^{-\mathrm{T}} + \mathbf{F}^{-1} \cdot \mathbf{k} \cdot \Delta_{\mathbf{d}}[\mathbf{F}^{-\mathrm{T}}] \right) \cdot \nabla_{\mathbf{X}}T \ \mathrm{d}\Omega - \int_{\mathcal{B}_0} \hat{\mathbf{N}}^{\mathrm{T}} \frac{T}{\Delta t}\mathbf{Z}^{\mathrm{T}}\mathbf{B} \ \mathrm{d}\Omega, \tag{62a}$$

$$\mathbf{K}_{T\varsigma} = -\int_{\mathcal{B}_0} \hat{\mathbf{N}}(\boldsymbol{\xi})^{\mathrm{T}} \frac{T}{\Delta t}\mathbf{Z}^{\mathrm{T}}\mathbf{M}(\boldsymbol{\xi}) \ \mathrm{d}\Omega; \tag{62b}$$

$$\mathbf{K}_{T\mathfrak{d}} = -\int_{\mathcal{B}_0} -2(1-\mathfrak{d})\hat{\mathbf{N}}(\boldsymbol{\xi})^{\mathrm{T}}(\mathbf{Z}^{\mathrm{T}}\dot{\mathbf{E}})\mathbf{N}(\boldsymbol{\xi}) \ \mathrm{d}\Omega, \tag{62c}$$

$$\mathbf{K}_{TT} = \int_{\mathcal{B}_0} \hat{\mathbf{N}}(\boldsymbol{\xi})^{\mathrm{T}}\frac{c_p}{\Delta t}\hat{\mathbf{N}}(\boldsymbol{\xi}) \ \mathrm{d}\Omega - \int_{\mathcal{B}_0} g(\mathfrak{d})\hat{\mathbf{N}}(\boldsymbol{\xi})^{\mathrm{T}}(\mathbf{Z}^{\mathrm{T}}\dot{\mathbf{E}})\hat{\mathbf{N}}(\boldsymbol{\xi}) \ \mathrm{d}\Omega + \int_{\mathcal{B}_0} J\mathbf{B}_T^{\mathrm{T}}\mathbf{F}^{-1} \cdot \mathbf{k} \cdot \mathbf{F}^{-\mathrm{T}}\mathbf{B}_T \ \mathrm{d}\Omega. \tag{62d}$$

Here, $\mathbf{K}_{\mathbf{dd},\mathrm{geom}}$ refers to the geometric contribution and the $\mathbf{K}_{\mathbf{dd},\mathrm{mat}}$ is the material contribution. Also, $\Delta_{\mathbf{d}}[J]$ and $\Delta_{\mathbf{d}}[\mathbf{F}^{-1}]$ and $\Delta_{\mathbf{d}}[\mathbf{F}^{-\mathrm{T}}]$ represents the linearization with respect to the kinematic field of the Jacobian J of the transformation $\mathbf{F}$, the inverse of the modified deformation gradient and its transpose, respectively, which lead to additional geometrical terms, see Appendix A, for the detailed computation of these terms. The overall algorithm of the implementation can be found in our recent article [26] (without phase-field). The implementation of the phase-field to the model mentioned in [26] is straightforward keeping in mind the Appendix A and the mathematical model presented in the article.

Since inter-element continuity is not required for enhanced strains, as in [56], they can be condensed out at the element level via a standard condensation process. Thus, the condensed version of the stiffness matrix given in Eq.(58) reads

$$\begin{bmatrix} \mathbf{K}_{\mathbf{dd}}^* & \mathbf{K}_{\mathbf{d}\tilde{\mathfrak{d}}}^* & \mathbf{K}_{\mathbf{d}T}^* \\ \mathbf{K}_{\tilde{\mathfrak{d}}\mathbf{d}}^* & \mathbf{K}_{\tilde{\mathfrak{d}}\tilde{\mathfrak{d}}}^* & \mathbf{K}_{\tilde{\mathfrak{d}}T}^* \\ \mathbf{K}_{T\mathbf{d}}^* & \mathbf{K}_{T\tilde{\mathfrak{d}}}^* & \mathbf{K}_{TT}^* \end{bmatrix} \begin{bmatrix} \Delta\mathbf{d} \\ \Delta\mathfrak{d} \\ \Delta\hat{\boldsymbol{T}} \end{bmatrix} = \begin{bmatrix} \tilde{\hat{\mathcal{R}}}^{\mathbf{d}} \\ \tilde{\hat{\mathcal{R}}}^{\mathfrak{d}} \\ \tilde{\hat{\mathcal{R}}}^{T} \end{bmatrix} \tag{63}$$

where the element stiffness contribution takes the form

$$\mathbf{K}_{\mathbf{dd}}^* = \mathbf{K}_{\mathbf{dd}} - \mathbf{K}_{\mathbf{d}\varsigma}\mathbf{K}_{\varsigma\varsigma}^{-1}\mathbf{K}_{\varsigma\mathbf{d}}; \quad \mathbf{K}_{\mathbf{d}\tilde{\mathfrak{d}}}^* = \mathbf{K}_{\mathbf{d}\tilde{\mathfrak{d}}} - \mathbf{K}_{\mathbf{d}\varsigma}\mathbf{K}_{\varsigma\varsigma}^{-1}\mathbf{K}_{\varsigma\tilde{\mathfrak{d}}}; \quad \mathbf{K}_{\mathbf{d}T}^* = \mathbf{K}_{\mathbf{d}T} - \mathbf{K}_{\mathbf{d}\varsigma}\mathbf{K}_{\varsigma\varsigma}^{-1}\mathbf{k}_{\varsigma T},$$
$$\mathbf{K}_{\tilde{\mathfrak{d}}\mathbf{d}}^* = \mathbf{K}_{\tilde{\mathfrak{d}}\mathbf{d}} - \mathbf{K}_{\tilde{\mathfrak{d}}\varsigma}\mathbf{K}_{\varsigma\varsigma}^{-1}\mathbf{k}_{\varsigma\tilde{\mathfrak{d}}}; \quad \mathbf{K}_{\tilde{\mathfrak{d}}\tilde{\mathfrak{d}}}^* = \mathbf{K}_{\tilde{\mathfrak{d}}\tilde{\mathfrak{d}}} - \mathbf{K}_{\tilde{\mathfrak{d}}\varsigma}\mathbf{K}_{\varsigma\varsigma}^{-1}\mathbf{K}_{\varsigma\tilde{\mathfrak{d}}}; \quad \mathbf{K}_{\mathbf{d}T}^* = \mathbf{K}_{\tilde{\mathfrak{d}}T} - \mathbf{K}_{\tilde{\mathfrak{d}}\varsigma}\mathbf{K}_{\varsigma\varsigma}^{-1}\mathbf{K}_{\varsigma T},$$
$$\mathbf{K}_{T\mathbf{d}}^* = \mathbf{K}_{T\mathbf{d}} - \mathbf{K}_{T\varsigma}\mathbf{K}_{\varsigma\varsigma}^{-1}\mathbf{k}_{\varsigma\mathbf{d}}; \quad \mathbf{K}_{T\tilde{\mathfrak{d}}}^* = \mathbf{K}_{T\tilde{\mathfrak{d}}} - \mathbf{K}_{T\varsigma}\mathbf{K}_{\varsigma\varsigma}^{-1}\mathbf{K}_{\varsigma\tilde{\mathfrak{d}}}; \quad \mathbf{K}_{TT}^* = \mathbf{K}_{TT} - \mathbf{K}_{T\varsigma}\mathbf{K}_{\varsigma\varsigma}^{-1}\mathbf{K}_{\varsigma T}, \tag{64}$$

along with the residual force vectors

$$\tilde{\hat{\mathcal{R}}}^{\mathbf{d}} = \hat{\mathcal{R}}_{\mathrm{ext}}^{u} - \hat{\mathcal{R}}_{\mathrm{int}}^{u} + \mathbf{K}_{\mathbf{d}\varsigma}\mathbf{K}_{\varsigma\varsigma}^{-1}\hat{\mathcal{R}}_{\mathrm{int}}^{\varsigma}$$
$$\tilde{\hat{\mathcal{R}}}^{\mathfrak{d}} = -\hat{\mathcal{R}}_{\mathrm{int}}^{\mathfrak{d}} + \mathbf{K}_{\mathfrak{d}\varsigma}\mathbf{K}_{\varsigma\varsigma}^{-1}\hat{\mathcal{R}}_{\mathrm{int}}^{\varsigma}$$
$$\tilde{\hat{\mathcal{R}}}^{T} = \hat{\mathcal{R}}_{\mathrm{ext}}^{T} - \hat{\mathcal{R}}_{\mathrm{int}}^{T} + \mathbf{K}_{T\varsigma}\mathbf{K}_{\varsigma\varsigma}^{-1}\hat{\mathcal{R}}_{\mathrm{int}}^{\varsigma} \tag{65}$$

The resulting system of algebraic equations in Eq.(63) can be solved using monolithic/staggered solution scheme using different types of solvers such as nonlinear Newton-Raphson, quasi-Newton based solvers such as Broyden–Fletcher–Goldfarb–Shanno (BFGS), coupled displacement solvers, etc.

Regarding the numerical implementation, the fully staggered scheme is used for the solution of the coupled problem. The coupled terms with respect to the damage variable $\mathfrak{d}$ is suppressed owing to the staggered scheme implementation. i.e, $\mathbf{K}_{d\varsigma}, \mathbf{K}_{dT}, \mathbf{K}_{T\varsigma}, \mathbf{K}_{T\tilde{\mathfrak{d}}}, \mathbf{K}_{\tilde{\mathfrak{d}}T}, \mathbf{K}_{\tilde{\mathfrak{d}}\varsigma}\mathbf{K}_{\varsigma T} = 0$. Moreover, it was noticed that normal newton solver performs better in the sense of convergence at each time step when the coupled problems involves. Whereas, for the problem without non-linearity (geometric), BFGS performed better. Meaning that, When the geometric non-linearity is involved BFGS takes longer time to converge at each

Material	E (MPa)	ν	$\alpha(10^{-6}/^oK)$	$k_0(W/mm^oK)$	$c_p(kJ/kg^oK)$	G_c (MPa$\sqrt{mm}$)	l (mm)
Silicon	1.69×10^5	0.16	1.1	0.114	0.715	0.014394	0.05
Alumina	2.1×10^5	0.31	10.1	5.05	0.4	0.32	0.2
Zircona	3.8×10^5	0.26	7.7	25	0.880	0.06634	0.2

Table 1: Properties of the simulated materials.

time step. The comparison between the solvers in terms of CPU times or iteration is out of scope for this article. See [79–82] for details regarding the BFGS implementation, merits, applications and capabilities. In the Numerical application section, Temperature assisted fracture in Section 4.2 and Plate with notch and many holes in Section 4.4 are solved using BFGS scheme, whereas, the other examples are solved using newton solver. Note that, the choice of solution scheme mentioned above is just to show that both solvers can be used in the solution scheme.

4. Numerical applications

In this section, the capabilities of the proposed phase-field model for thermo-mechanical solid shell formulation are assessed according to several representative examples. First, a benchmark test is proposed and passed. Then, problems characterized by temperature-assisted fracture are examined in relation to a technological phenomenon relevant for silicon solar cells. Finally, examples concerning coupled mechanical-temperature effects, for small and large strain problems are shown for a series of structural problems with plates and curved shells. In order to show examples spanning the wide range of material behaviour (especially temperature effects), three different materials are considered in Tab.1. There, E is the Young's Modulus, ν is the Poisson's ratio, α is the co-efficient of thermal expansion, k_0 is the thermal conductivity, c_p is heat capacity, G_c is the fracture energy, and l is the length scale of the phase field model.

4.1. Verification example: double-edged notch

This example concerns with the application of the proposed model to a double-edged notched specimen. Fig 3 shows the sketch of the model with an initial notch length $a = 0.1$ mm, axial length $L = 1$ mm, width $w = 0.5$ mm and thickness $h = 0.01$ mm in line with the numerical experiment of [83] and has been studied by [84] by considering the alumina whose material properties are given in Tab. 1 Here, we have used the length scale $l = 0.0075$ mm in line with the experiments in [83]. The model is discretized with 812 elements such that element size of $2l$ is maintained at the crack path.

The displacement load of $\Delta = 0.01$ mm is applied in 1000 steps on the top surface, and the bottom surface is fully restrained. The EAS and ANS are included in the whole domain but are turned off locally when the damage variable reaches $\mathfrak{d} = 0.5$ due to unstable crack propagation in the system.

Note that, due to the scarcity of thermo-mechanical crack propagation experiments, the comparison has been made based on standard examples proposed in [83]. In line with the numerical example reported in [83], where the temperature dependency is null, the temperature of the whole model is kept at $T = 0^oC$, which means that no external boundary temperature is inflicted upon the model. It can be argued that the local temperature T_0 is different from zero. Still, it is noticed that, numerically, the difference arises due to the difference between the initial temperature and the externally applied temperature rather than the absolute values. Hence, the all local temperatures are kept at T_0 for comparison.

The load-displacement curve for the evolution of the simulation shows a satisfactory agreement with the experimental results as in Fig. 3. The numerical experiments conducted in [83] consider the plane strain condition whose thickness is 1 mm. To match that, the reactions forced are multiplied by a factor of 100 since the thickness considered here is $h = 0.01$ mm.

The evolution of the phase-field variable $\mathfrak{d}$ at displacement just before and after the damage is shown in Fig. 3. This example is complemented by adding the thermal effect. For doing that, we select a temperature gradient within the domain, see the corresponding load-displacement evolution curves corresponding in Fig. 4(a). It can be readily seen that as the temperature increases, the maximum load-bearing capacity of the
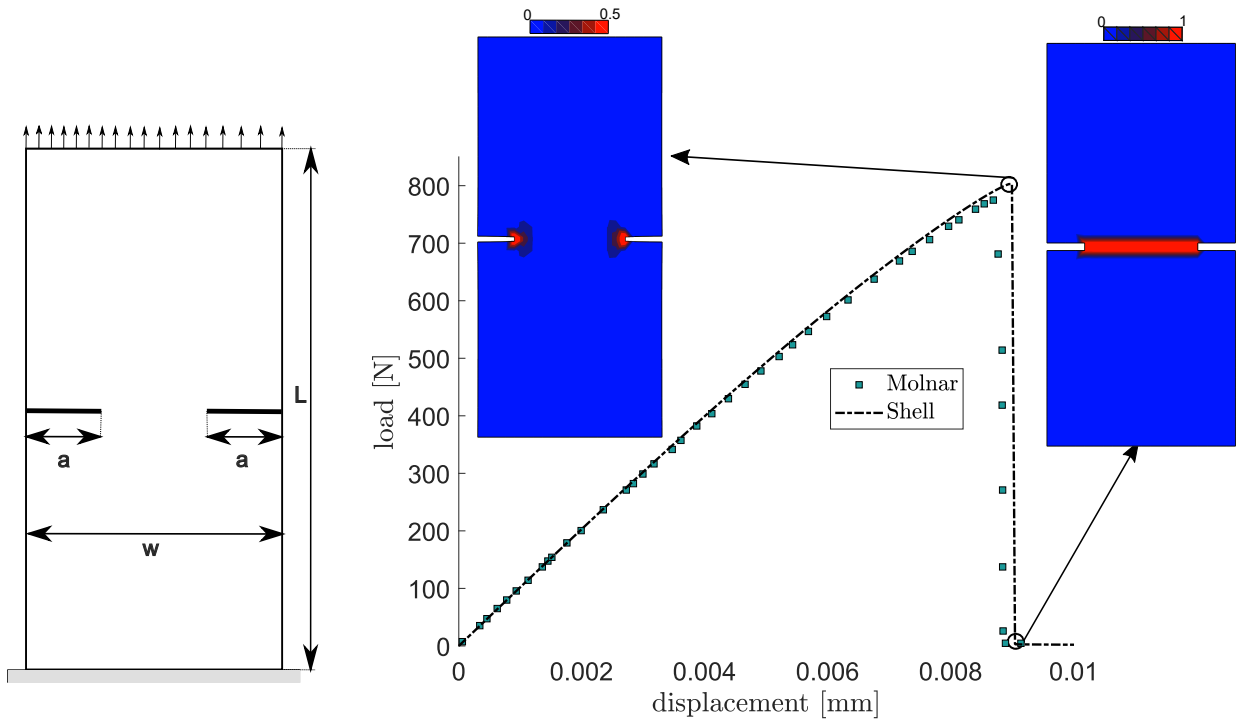
Figure 3: Verification example: geometry and force reaction-displacement evolution curve.
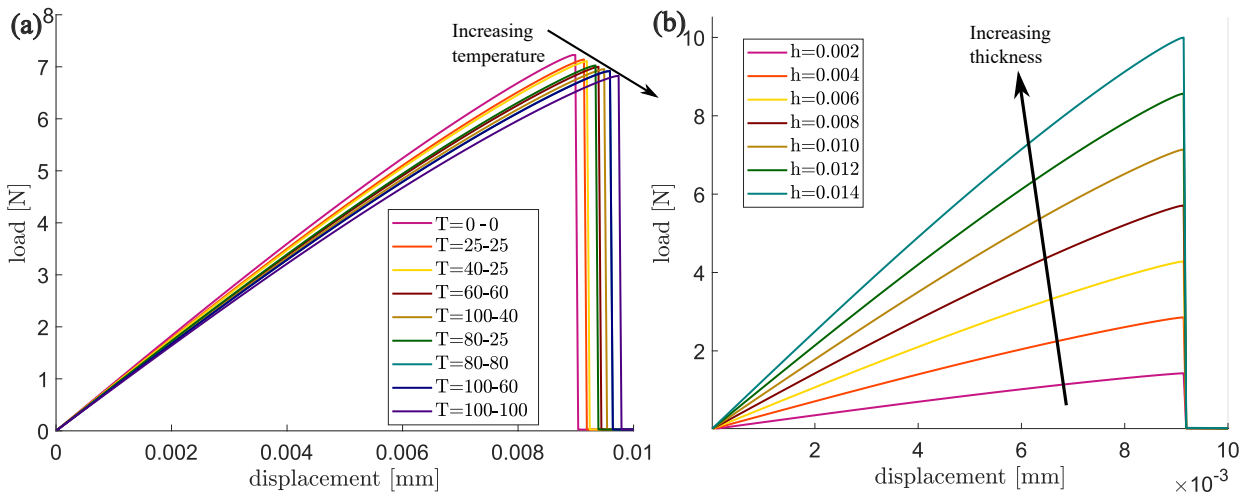

Figure 4: Double-edged notch specimen with (a) reactions for variation of temperatures, (b) reactions for variation of thickness
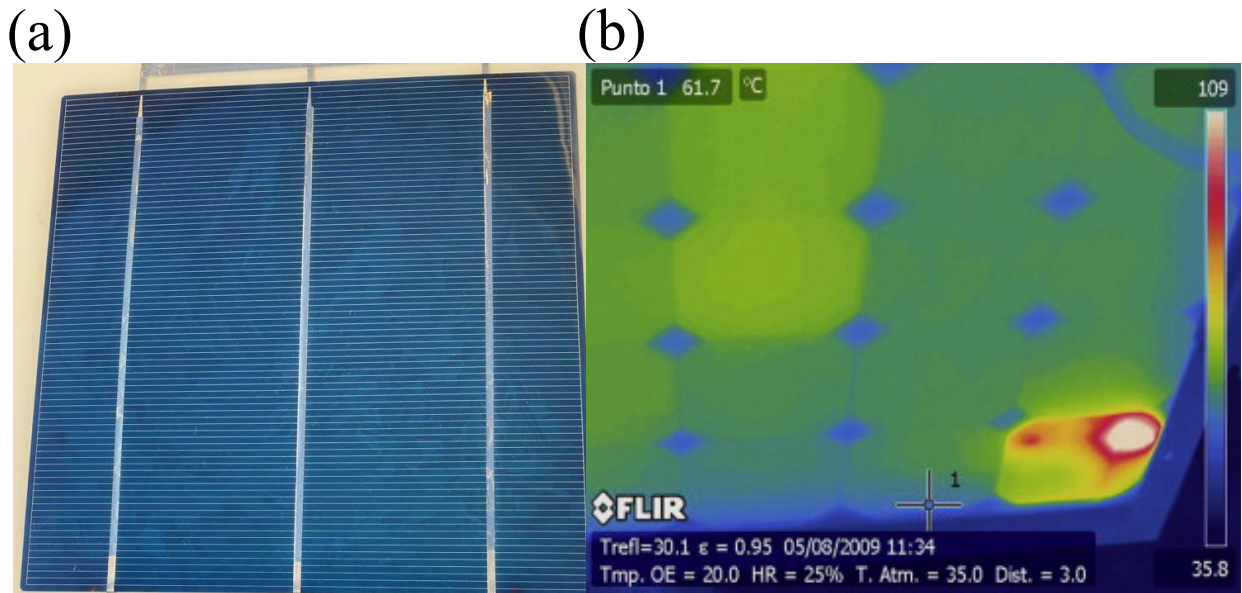
Figure 5: (a) Solar panel with bus bar (b) Thermal images from thermal camera showing the local temperature rises (hot spots) in silica cells in case of cracks, adopted from [85].

model decreases. Keeping the temperature boundary conditions ($T = 25^0 - 25^0$C) and the material properties constants, the thickness variation in the plate is considered. It is noticed that, as the thickness increases, the load-bearing capacity of the specimen increases, as shown in Fig. 4(b). It can be seen from Fig. 4(b) that there exists a direct linear mapping between the different variations of thickness. Meaning that, if load-displacement (say $F_1(t)$) curve for thickness h_1 is known, then for any thickness h_2, the load-displacement curve can be obtained from h_1 as $F_2(t) = F_1(t)\dfrac{h_2}{h_1}$.

4.2. Application to photo-voltaic panels: temperature assisted fracture

In this example, the proposed model is used to investigate the effects of cracking in silicon used for solar cells. Experimental results [85] and the numerical investigation [86] show that silicon defects may induce hot spots in solar cells. This phenomenon may enhance cracking, degrade the photovoltaic performance of the device, and eventually lead to safety issues.

Following [86, 87], it is discussed that during the manufacturing of a solar cell module, crack-free cells made of mono/poly-crystalline silicon are laminated inside a stack formed of an encapsulating polymer and a cover glass at a temperature around $T_0 = 150^oC$. Later, the module is cooled down to the ambient temperature with a final state with residual compressive stresses.Fig. 5(a) represents the solar cell with the glass laminate. A local temperature increase is thermal images, see Fig. 5(b) (adapted from [85]). The thermo-elastic displacement caused by these conditions Fig. 5(a) in the solar cells can induce fracture.

As an model example, a mono-crystalline silicon solar cell without any pre-existing crack is considered with properties as in Tab 1. The model is discretized with 16512 equidistant elements. The cell boundary $\partial\Omega$ is subdivided into $\partial\Omega_1$ and $\partial\Omega_2$, restrained as in Fig. 6(a). A temperature excursion $\Delta T_1 = -30^oC$ is herein considered along $\partial\Omega_1$ to depict a temperature raise as compared to the other portion of the boundary, $\partial\Omega_2$, where we set $\Delta T_2 = -20^oC$ as for normal operative conditions. The temperatures are applied over 1000 steps linearly. The reference temperature is in both cases the stress-free lamination temperature T_0.

The above non-linear heat conduction problem is solved using the proposed model, to simulate temperature-assisted fracture induced by the thermo-mechanical displacement field. The evolution of the phase-field variable along with the temperature distribution inside the cell is shown in Fig. 7(right). When the crack
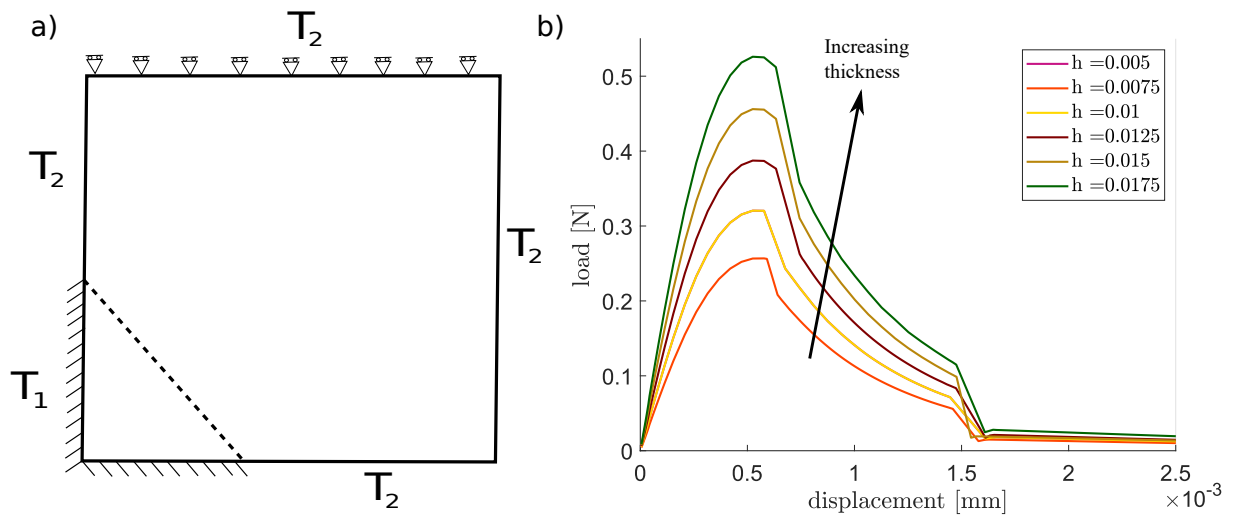
16

Figure 6: (a) Model under consideration (b) Load-displacement curve for different solar cell thickness.
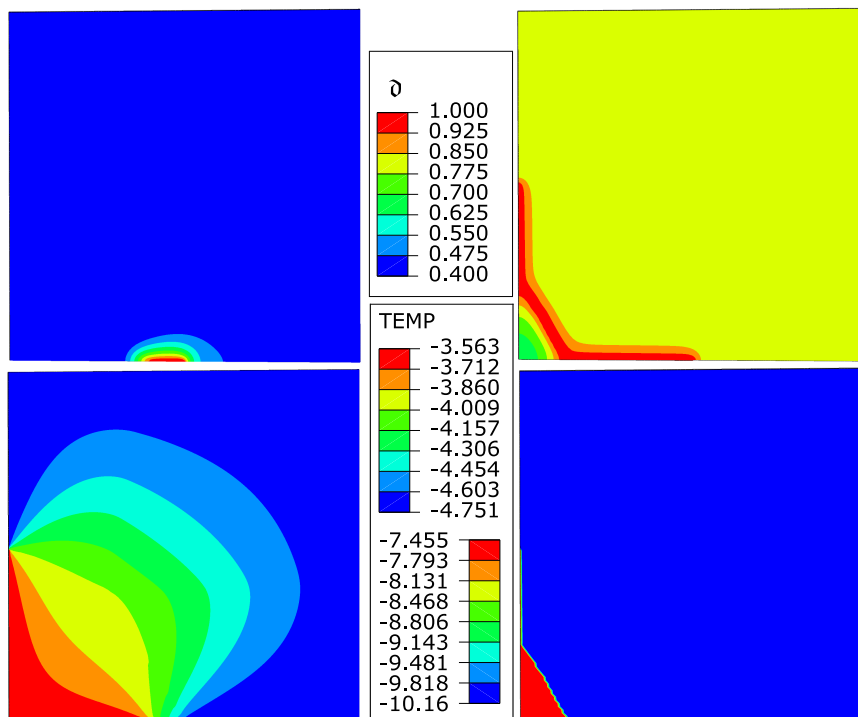

Figure 7: Temperature assisted fracture. (left) Figure on left represents phase-field and temperature distribution during initiation of fracture at step 118. (right) Fig on right represents phase-field and temperature distribution after the fracture at step 251.
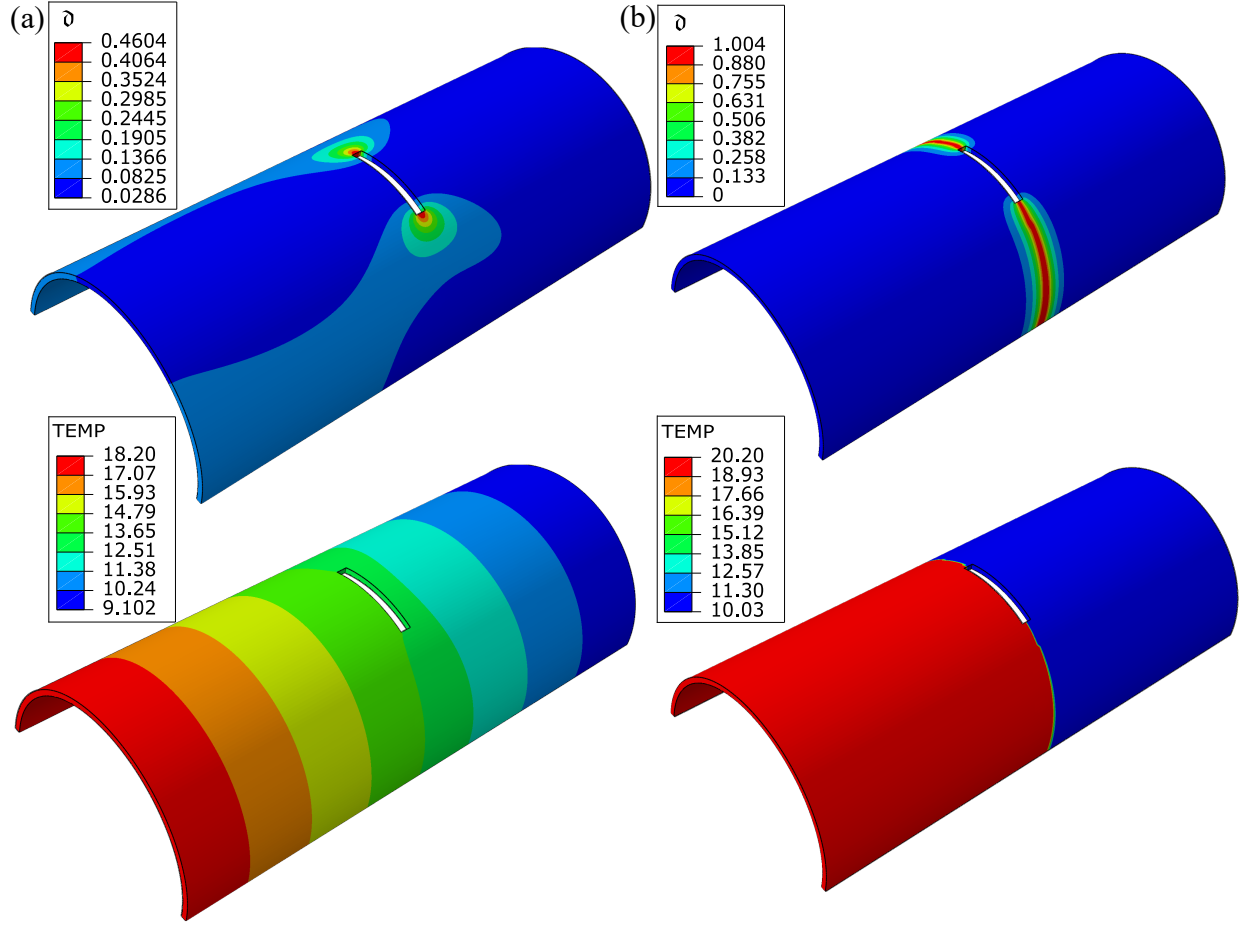
Figure 8: (a) Phase-field and temperature distribution for a cylindrical shell with a notch before crack at displacement load of $\Delta = 2.9 \times 10^{-3}$ mm, (b) Phase-field and temperature distribution after crack propagation at displacement load of $\Delta = 3.2 \times 10^{-3}$ mm.

is fully propagated, it acts as a thermal barrier for heat transfer across the solar cell and the temperature becomes uniform in the two separated regions of the material. The load-displacement curve for the evolution of the damage is shown in Fig. 6(b) for different thicknesses of the solar cell. Analogous to the verification example, as the thickness increases, the load-bearing capacity increases. Moreover, It can be noticed that there exists a direct linear mapping of the load-displacement curves with the thickness as in the verification example.

4.3. Notched cylinder under tensile loading: curved shells application

In this example, a cylindrical shell is considered. In particular, two cases are considered (a) a cylindrical shell with an initial notch and (b) a cylindrical shell with a hole for sheets of alumina with material properties as detailed in Tab 1.

For the cylindrical shells with a notch, the geometrical description of the model considers a radius of the cylinder $R = 2$ mm, length $L = 10$ mm, thickness $h = 0.01$ mm with notch in the centre whose arc length is 1.5 mm such that the notch spans $\theta = 21.5^o$ each side. The model is discretized with 24339 elements with maximum element size is at least $2l$.

One axial end of the cylinder is fixed, whereas a monotonic prescribed axial displacement is applied on the opposite end. Temperatures of $T_1 = 50^o$C and $T_2 = 25^o$C are applied on fixed end and on the loaded

18
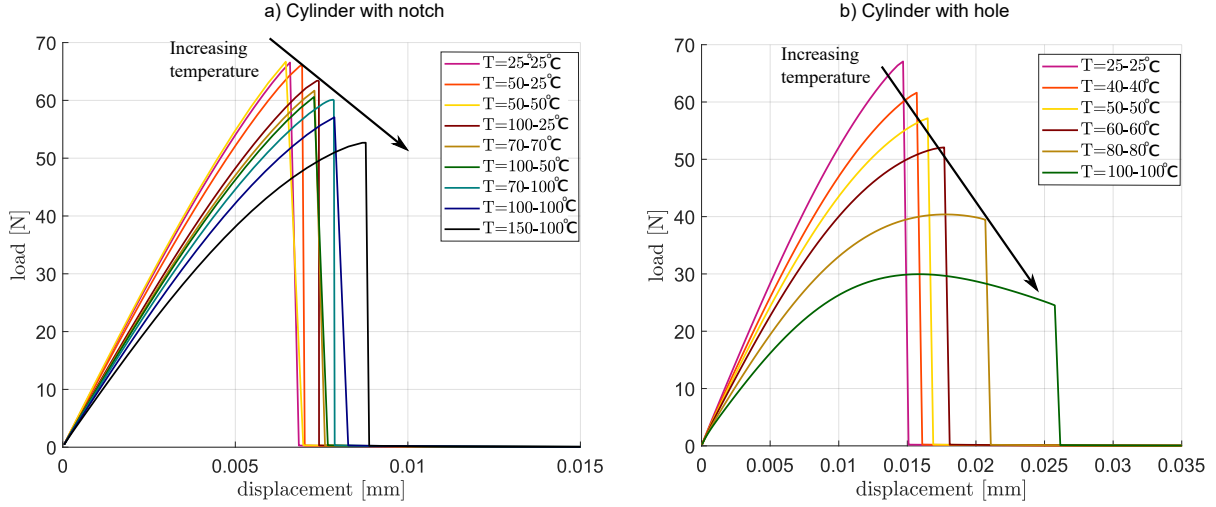
Figure 9: Force vs displacement curve for (a) cylinder with notch, and (b) cylinder with hole.

ends, respectively. The ambient temperature is kept at $T_0 = 0^oC$. Fig. 8(a) shows the evolution of the phase-field ($\mathfrak{d}$) and temperature corresponding to the displacement $\Delta = 0.016$ mm. It can be observed that the temperature is linearly distributed along the cylinder length, until it breaks in two parts due to fracture, which again leads to heat flux insulation across the corresponding generated crack surface.

Along with the base model, Fig. 9(a) shows the variation of load-displacement curves for various temperature boundary conditions. It can be seen from Fig. 9(a) that as the temperature increases, the load-carrying capacity of the model decreases.

For the case of the cylinder including the central hole, the geometrical description of the model follows the radius of $R = 2$ mm, length $L = 20$ mm with thickness $h = 0.01$ mm with hole in the centre with radius $r = 0.15$ mm. The model is discretized with 12491 elements with maximum element size is at least $2l$. For similar boundary conditions as before, but with $T_1 = T_2 = 25^oC$ (Base Model), the phase-field and the temperature distribution before ($\Delta = 0.016$ mm) and after the fracture ($\Delta = 0.016$ mm) are shown in Fig. 10(a) and Fig. 10(b) respectively. Along with the base model, the load-displacement curve for the variation of different boundary conditions $T_1 = T_2$ are shown in Fig. 9(b). As in the case with cylinder with notch, as the temperature increases, the load carrying capacities of the cylinder decreases.

4.4. Plate with notch and multiple holes

In this example, a plate with multiple holes and an eccentric notch is considered to show stable crack propagation. A Zircona plate (with properties as in Tab. 1) of length $L = 120$ mm, width $w = 60$ mm and thickness $h = 1$ mm is considered as shown in Fig. 11(a). The model is discretized with approximately 6000 elements with finer mesh near the crack path. The bottom surface is fully restrained, whereas the displacement boundary of $\Delta = 0.1$mm is applied on the top surface as shown in Fig. 11(a). The temperature of 30^oC is applied on the top and bottom surfaces, whereas a temperature of 25^oC is applied on both sides of the plate. The evolution of the temperature and the phase-field along with the reactions are presented in Fig. 11(b). The phase-field evolution during the initiation, propagation (snapback), and the complete damage is shown in 11(b). The temperature distribution at the end of time step ($t = 1$, $\Delta = 0.1$mm) is shown in 11(b). It can be seen that, due to the existence of centre hole, the crack starts from the notch, and propagate only until centre hole. The temperature starts to diffuse inwards whereas at the path of crack, temperature is higher. Later, as the load increases, the crack travel further leading to complete failure. Temperature distribution reflects the applied temperature and the crack propagation.
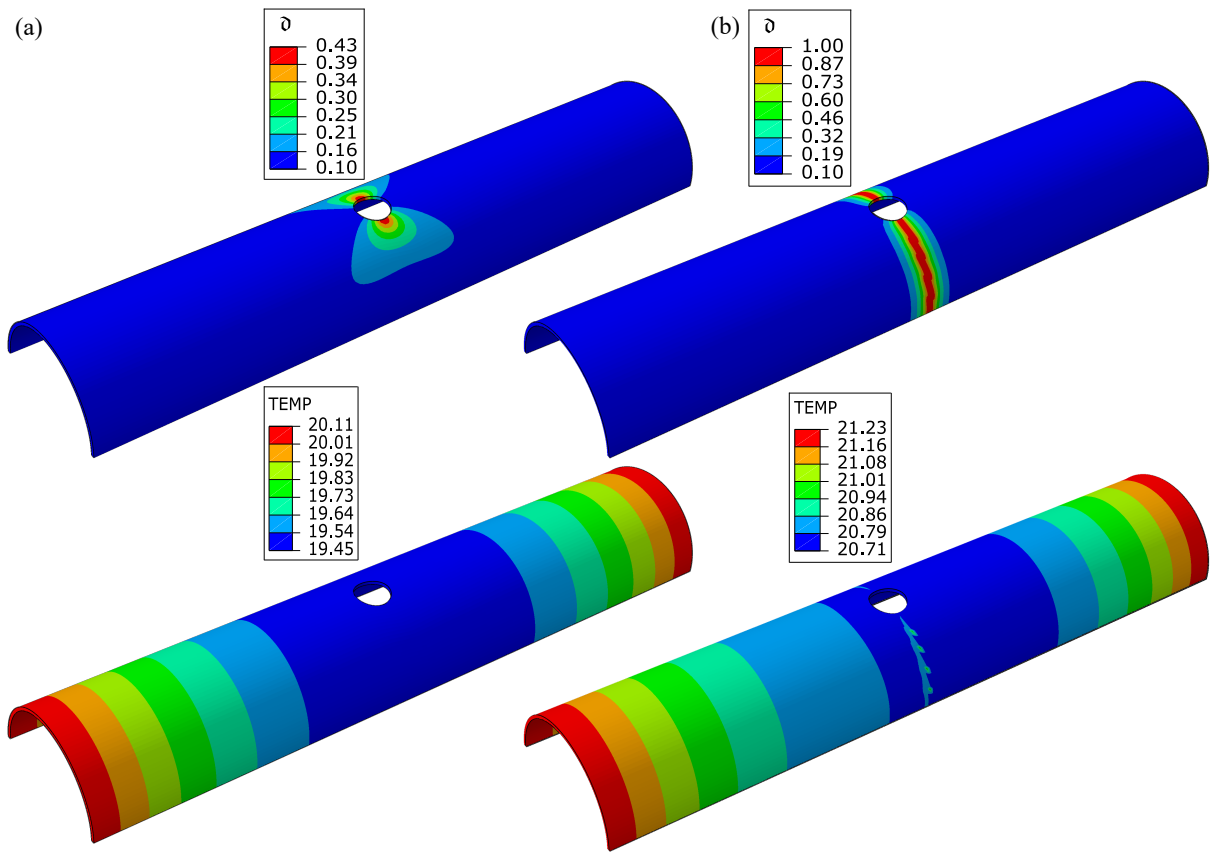
19

Figure 10: (a) Phase-field and temperature distribution for a cylindrical shell with a hole before crack at displacement load of $\Delta = 1.4 \times 10^{-2}$mm, (b) Phase-field and temperature distribution after crack propagation at displacement load of $\Delta = 1.5 \times 10^{-2}$mm.
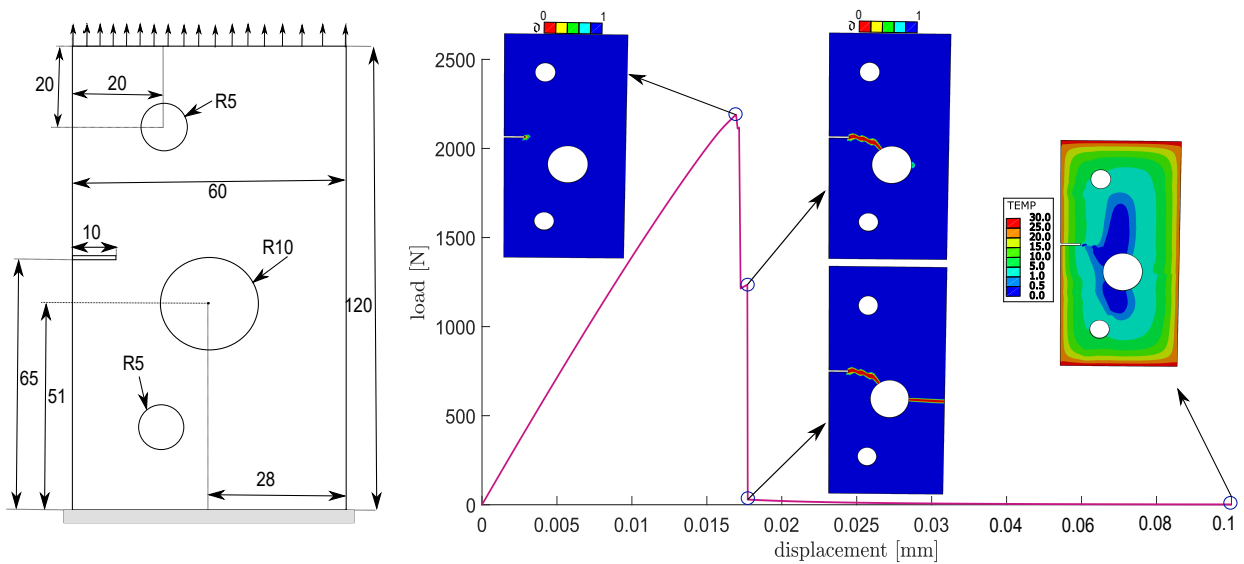

Figure 11: Phase-field and temperature distribution for plate with notch and hole along with reactions.

5. Concluding remarks

In this work, a thermodynamically consistent derivation of thermo-mechanical locking free solid shell with full integration capable of handling large strains has been proposed. Locking effects are alleviated using the combination of 7 EAS parameters and the ANS method.

The numerical predicting capabilities of the model are explored with three different materials having extremely different thermal and mechanical properties, namely: (a)silicon, (b)alumina, and (c) zircona.

The model is validated against the benchmark example of a double-edged notch of alumina to demonstrate the predictive capabilities of the model. Furthermore, the model has been shown to predict temperature assisted fracture using a model silicon cell. It has been also shown that due to the difference in temperature, the crack develops and the presence of crack induces insulated barriers to heat flux. Cylinder with notch and cylinder with hole is shows that there is no locking and effect of temperature in the fracture. From the numerical experiments, it is shown that as the cumulative temperature increases, the maximum load bearing capacity decreases. Correspondingly, the examples have shown that temperature distributions may lead to fracture and, conversely, cracks may affect the temperature distribution. Plate with notch and multiple holes shows the model ability to predict stable crack propagation.

Finally, it can be emphasized that the developed model is particularly promising in addressing a wide range of industrial problems in automotive (body, chassis), aerospace (wings, turbines blades, rudder), renewable energy (photovoltaics, electronic chips, screen protectors, etc.) and thermal barrier coatings involving thick/thin plates (straight and curved) where temperature effects are significant.

Appendix A. Computation implementation details

This sections summarises the discrete form of several operators that are important in the numerical implementation but are not straightforward in the current solid shell element. The curvilinear basis vector in the current configuration reads

$$\mathbf{g}_i = \qquad \frac{\partial \mathbf{x}}{\partial \xi^i} = \mathbf{G}_i + \frac{\partial \mathbf{u}}{\partial \xi^i}, \tag{A.1}$$

$$\approx \quad \sum_{j=1}^{n_n} N^{j,\xi^i}(\boldsymbol{\xi}) \begin{bmatrix} x_i \\ y_i \\ z_i \end{bmatrix} + \sum_{j=1}^{n_n} N^{j,\xi^i}(\boldsymbol{\xi}) \begin{bmatrix} d_{i,x} \\ d_{i,y} \\ d_{i,z} \end{bmatrix}, \tag{A.2}$$

with $i = 1, 2, 3$ and $N^{j,\xi^i}(\boldsymbol{\xi}) = \dfrac{\partial N^j(\boldsymbol{\xi})}{\partial \xi^i}$.

The $\mathbf{B}(\mathbf{d})$ in the Eq. (45) requires the computation of partial derivative of covariant basis $\mathbf{g_i}$ in current configuration with respect to discrete displacement vector $\mathbf{d}_j$ takes the form

$$\mathbf{B}(\mathbf{d}) = \frac{\partial \mathbf{g_i}}{\partial \mathbf{d}_j} = \begin{bmatrix} \dfrac{\partial \mathbf{g_{i,x}}}{\partial \mathbf{d}_j} \\ \dfrac{\partial \mathbf{g_{i,y}}}{\partial \mathbf{d}_j} \\ \dfrac{\partial \mathbf{g_{i,z}}}{\partial \mathbf{d}_j} \end{bmatrix} = \begin{bmatrix} N^{j,\xi^i}(\boldsymbol{\xi}) & 0 & 0 \\ 0 & N^{j,\xi^i}(\boldsymbol{\xi}) & 0 \\ 0 & 0 & N^{j,\xi^i}(\boldsymbol{\xi}) \end{bmatrix}, \tag{A.3}$$

with $i = 1, 2, 3$ and $j = \{1, 8\}$.

The geometric contribution in the stiffness matrix $\mathbf{K_{dd}},\text{geom}$ in Eq. (??) incorporates the partial derivative of the $B-$operator with respect to the kinematic displacement field as

$$\mathbf{K_{dd}},\text{geom} = \delta\mathbf{d}\left[\left[\frac{\partial \mathbf{B}(\mathbf{d})}{\partial \mathbf{d}}\right]^{\mathrm{T}} \mathbf{S}\right] = \sum_{i=1}^{n}\sum_{j=1}^{n} \delta\mathbf{d}_i^T \mathcal{H}_i j \Delta\mathbf{d}_j^T, \tag{A.4}$$

with

$$\mathcal{H}_i j = S^{11} N^{i,\xi^1} N^{j,\xi^1} + S^{22} N^{i,\xi^2} N^{j,\xi^2} + S^{33} N^{i,\xi^3} N^{j,\xi^3} + S^{12}\left(N^{i,\xi^1} N^{j,\xi^2} + N^{i,\xi^2} N^{j,\xi^1}\right) \tag{A.5}$$

$$+ S^{13}\left(N^{i,\xi^1} N^{j,\xi^3} + N^{i,\xi^3} N^{j,\xi^1}\right) + S^{23}\left(N^{i,\xi^2} N^{j,\xi^3} + N^{i,\xi^3} N^{j,\xi^2}\right). \tag{A.6}$$

Note that, in the sequel, the stress operator $\mathbf{S}$ has to be modified according to ANS.

In the curvilinear setting, the linearization of the determinant of deformation gradient in Eq. (??) is expressed as

$$\Delta_{\mathbf{d}}[J] = J\mathbf{F}^{-\mathrm{T}} : \Delta\mathbf{F} = J(\mathbf{g}^i \otimes \mathbf{G}_i) : (\Delta\mathbf{g}_m \otimes \mathbf{G}^m) = J(\mathbf{g}^i \cdot \Delta\mathbf{g}_m)\delta_i^m = J(\mathbf{g}^i \cdot \Delta\mathbf{g}_i). \tag{A.7}$$

The linearization of the covariant basis vectors $\Delta_{\mathbf{d}}\mathbf{g}_m$ in Eq. (??) in the current configuration can be estimated by means of a suitable operator $\mathbf{B}_m^{(g)}$, which renders

$$\Delta_{\mathbf{d}}\mathbf{g}_m = \mathbf{B}_m^g \Delta\mathbf{d} = \begin{bmatrix} \frac{\partial N^1}{\partial \xi^m} & 0 & 0 & \cdots & \frac{\partial N^8}{\partial \xi^m} & 0 & 0 \\ 0 & \frac{\partial N^1}{\partial \xi^m} & 0 & \cdots & 0 & \frac{\partial N^8}{\partial \xi^m} & 0 \\ 0 & 0 & \frac{\partial N^1}{\partial \xi^m} & \cdots & 0 & 0 & \frac{\partial N^8}{\partial \xi^m} \end{bmatrix} \Delta\mathbf{d}. \tag{A.8}$$

The linearization of the inverse of the deformation gradient $\Delta_{\mathbf{d}}[\mathbf{F}^{-1}]$ and the related computation in Eq. (??) can be expressed as

$$\Delta_{\mathbf{d}}[\mathbf{F}^{-1}] = \mathbf{F}^{-1}\Delta_{\mathbf{d}}[\mathbf{F}]\mathbf{F}^{-1} = \left(\mathbf{G}_i \otimes \mathbf{g}^i\right)\left(\Delta\mathbf{g}_k \otimes \mathbf{G}^k\right)\left(\mathbf{G}_m \otimes \mathbf{g}^m\right) = \left(\mathbf{g}^i \cdot \Delta\mathbf{g}_m\right)\left(\mathbf{G}_i \otimes \mathbf{g}^m\right), \tag{A.9}$$

then

$$\Delta_{\mathbf{d}}[\mathbf{F}^{-1}]\mathbf{k}\mathbf{F}^{-\mathrm{T}} = \left(\mathbf{g}^i \cdot \Delta\mathbf{g}_m\right)\left(\mathbf{G}_i \otimes \mathbf{g}^m\right)\left(k^{ab}\mathbf{g}_a \otimes \mathbf{g}_b\right)\left(\mathbf{g}^c \otimes \mathbf{G}^c\right) = \mathbf{g}^i \cdot \Delta\mathbf{g}_m k^{mc}\left(\mathbf{G}_i \otimes \mathbf{G}_c\right), \tag{A.10}$$

and

$$\mathbf{F}^{-1}\mathbf{k}\Delta_{\mathbf{d}}[\mathbf{F}^{-\mathrm{T}}] = \left(\mathbf{G}_i \otimes \mathbf{g}^i\right)\left(k^{mn}\mathbf{g}_m \otimes \mathbf{g}_n\right)\left(\Delta\mathbf{g}_a \cdot \mathbf{g}^b \mathbf{g}^a \otimes \mathbf{G}_b\right) = k^{ia}\Delta\mathbf{g}_a \cdot \mathbf{g}^b\left(\mathbf{G}_i \otimes \mathbf{G}_b\right). \tag{A.11}$$

References

[1] T. Rabczuk, G. Zi, A Meshfree Method based on the Local Partition of Unity for Cohesive Cracks, Computational Mechanics 39 (6) (2007) 743–760. doi:10.1007/s00466-006-0067-4.
URL https://doi.org/10.1007/s00466-006-0067-4

[2] J. Dolbow, N. Moës, T. Belytschko, Modeling fracture in mindlin–reissner plates with the extended finite element method, International Journal of Solids and Structures 37 (48) (2000) 7161–7183. doi:https://doi.org/10.1016/S0020-7683(00)00194-3.
URL https://www.sciencedirect.com/science/article/pii/S0020768300001943

[3] S. Natarajan, P. Baiz, S. Bordas, T. Rabczuk, P. Kerfriden, Natural frequencies of cracked functionally graded material plates by the extended finite element method, Composite Structures 93 (11) (2011) 3082–3092. doi:https://doi.org/10.1016/j.compstruct.2011.04.007.
URL https://www.sciencedirect.com/science/article/pii/S0263822311001310

[4] P. M. A. Areias, T. Belytschko, Non-linear analysis of shells with arbitrary evolving cracks using xfem, International Journal for Numerical Methods in Engineering 62 (3) (2005) 384–415. doi:https://doi.org/10.1002/nme.1192.
URL https://onlinelibrary.wiley.com/doi/abs/10.1002/nme.1192

[5] P. Areias, J.-H. Song, T. Belytschko, Analysis of fracture in thin shells by overlapping paired elements, Computer Methods in Applied Mechanics and Engineering 195 (2006) 5343–5360.

[6] T. Chau-Dinh, G. Zi, P.-S. Lee, T. Rabczuk, J.-H. Song, Phantom-node method for shell models with arbitrary cracks, Computers & Structures 92-93 (2012) 242–256. doi:https://doi.org/10.1016/j.compstruc.2011.10.021.
URL https://www.sciencedirect.com/science/article/pii/S0045794911002768

[7] F. Caleyron, A. Combescure, V. Faucher, S. Potapov, Dynamic simulation of damage-fracture transition in smoothed particles hydrodynamics shells, International Journal for Numerical Methods in Engineering 90 (6) (2012) 707–738. doi:https://doi.org/10.1002/nme.3337.
URL https://onlinelibrary.wiley.com/doi/abs/10.1002/nme.3337

[8] T. Rabczuk, P. M. A. Areias, T. Belytschko, A meshfree thin shell method for non-linear dynamic fracture, International Journal for Numerical Methods in Engineering 72 (5) (2007) 524–548. doi:https://doi.org/10.1002/nme.2013.
URL https://onlinelibrary.wiley.com/doi/abs/10.1002/nme.2013

[9] N. Nguyen-Thanh, N. Valizadeh, M. Nguyen, H. Nguyen-Xuan, X. Zhuang, P. Areias, G. Zi, Y. Bazilevs, L. De Lorenzis, T. Rabczuk, An extended isogeometric thin shell analysis based on kirchhoff–love theory, Computer Methods in Applied Mechanics and Engineering 284 (2015) 265–291, isogeometric Analysis Special Issue. doi:https://doi.org/10.1016/j.cma.2014.08.025.

[10] S. Mostofizadeh, M. Fagerström, R. Larsson, Dynamic crack propagation in elastoplastic thin-walled structures: Modelling and validation, International Journal for Numerical Methods in Engineering 96 (2) (2013) 63–86. doi:https://doi.org/10.1002/nme.4524.
URL https://onlinelibrary.wiley.com/doi/abs/10.1002/nme.4524

[11] P. M. Areias, J. Song, T. Belytschko, Analysis of fracture in thin shells by overlapping paired elements, Computer Methods in Applied Mechanics and Engineering 195 (41) (2006) 5343–5360, john H. Argyris Memorial Issue. Part II. doi:https://doi.org/10.1016/j.cma.2005.10.024.
URL https://www.sciencedirect.com/science/article/pii/S0045782505005475

[12] G. Becker, C. Geuzaine, L. Noels, A one field full discontinuous galerkin method for kirchhoff–love shells applied to fracture mechanics, Computer Methods in Applied Mechanics and Engineering 200 (45) (2011) 3223–3241. doi:https://doi.org/10.1016/j.cma.2011.07.008.
URL https://www.sciencedirect.com/science/article/pii/S0045782511002490

[13] A. Ahmed, F. van der Meer, L. Sluys, A geometrically nonlinear discontinuous solid-like shell element (dsls) for thin shell structures, Computer Methods in Applied Mechanics and Engineering 201-204 (2012) 191–207. doi:https://doi.org/10.1016/j.cma.2011.10.008.
URL https://www.sciencedirect.com/science/article/pii/S0045782511003203

[14] M. Pagani, U. Perego, Explicit dynamics simulation of blade cutting of thin elastoplastic shells using "directional" cohesive elements in solid-shell finite element models, Computer Methods in Applied Mechanics and Engineering 285 (2015) 515–541. doi:https://doi.org/10.1016/j.cma.2014.11.027.
URL https://www.sciencedirect.com/science/article/pii/S0045782514004538

[15] F. Cirak, M. Ortiz, A. Pandolfi, A cohesive approach to thin-shell fracture and fragmentation, Computer Methods in Applied Mechanics and Engineering 194 (21) (2005) 2604–2618, computational Methods for Shells. doi:https://doi.org/10.1016/j.cma.2004.07.048.

[16] P. D. Zavattieri, Modeling of Crack Propagation in Thin-Walled Structures Using a Cohesive Model for Shell Elements, Journal of Applied Mechanics 73 (6) (2005) 948–958. doi:10.1115/1.2173286.

[17] W. Li, T. Siegmund, An analysis of crack growth in thin-sheet metal via a cohesive zone model, Engineering Fracture Mechanics 69 (18) (2002) 2073–2093. doi:https://doi.org/10.1016/S0013-7944(02)00013-9.

[18] S. Forest, Micromorphic approach for gradient elasticity, viscoplasticity, and damage, Journal of Engineering Mechanics 135 (3) (2009) 117–131. doi:10.1061/(ASCE)0733-9399(2009)135:3(117).

[19] T. Waffenschmidt, C. Polindara, A. Menzel, S. Blanco, A gradient-enhanced large-deformation continuum damage model for fibre-reinforced materials, Computer Methods in Applied Mechanics and Engineering 268 (2014) 801–842. doi:https://doi.org/10.1016/j.cma.2013.10.013.

[20] R. H. J. PEERLINGS, R. DE BORST, W. A. M. BREKELMANS, J. H. P. DE VREE, Gradient enhanced damage for

quasi-brittle materials, International Journal for Numerical Methods in Engineering 39 (19) (1996) 3391–3403. `doi:https://doi.org/10.1002/(SICI)1097-0207(19961015)39:19<3391::AID-NME7>3.0.CO;2-D`.

[21] A. Dean, S. Sahraee, K. Ozenc, J. Reinoso, R. Rolfes, M. Kaliske, A thermodynamically consistent framework to couple damage and plasticity microplane-based formulations for fracture modeling: development and algorithmic treatment, International Journal of Fracture 203 (2016) 115–134. `doi:10.1007/s10704-016-0131-9`.

[22] M. Ambati, L. De Lorenzis, Phase-field modeling of brittle and ductile fracture in shells with isogeometric nurbs-based solid-shell elements, Computer Methods in Applied Mechanics and Engineering 312 (2016) 351–373, phase Field Approaches to Fracture. `doi:https://doi.org/10.1016/j.cma.2016.02.017`.

[23] F. Amiri, D. Millán, Y. Shen, T. Rabczuk, M. Arroyo, Phase-field modeling of fracture in linear thin shells, Theoretical and Applied Fracture Mechanics 69 (2014) 102–109, introducing the new features of Theoretical and Applied Fracture Mechanics through the scientific expertise of the Editorial Board. `doi:https://doi.org/10.1016/j.tafmec.2013.12.002`.

[24] J. Reinoso, M. Paggi, C. Linder, Phase field modeling of brittle fracture for enhanced assumed strain shells at large deformations: formulation and finite element implementation, Computational Mechanics 59 (6) (2017) 981–1001. `doi:10.1007/s00466-017-1386-3`.
URL `https://doi.org/10.1007/s00466-017-1386-3`

[25] J. Kiendl, M. Ambati, L. De Lorenzis, H. Gomez, A. Reali, Phase-field description of brittle fracture in plates and shells, Computer Methods in Applied Mechanics and Engineering 312 (2016) 374–394, phase Field Approaches to Fracture. `doi:https://doi.org/10.1016/j.cma.2016.09.011`.
URL `https://www.sciencedirect.com/science/article/pii/S0045782516311318`

[26] P. K. A. V. Kumar, A. Dean, S. Sahraee, J. Reinoso, M. Paggi, Non-linear thermoelastic analysis of thin-walled structures with cohesive-like interfaces relying on the solid shell concept, Finite Elements in Analysis and Design 202 (2022) 103696. `doi:https://doi.org/10.1016/j.finel.2021.103696`.
URL `https://www.sciencedirect.com/science/article/pii/S0168874X21001700`

[27] J. Kiendl, K.-U. Bletzinger, J. Linhard, R. Wüchner, Isogeometric shell analysis with kirchhoff–love elements, Computer Methods in Applied Mechanics and Engineering 198 (49) (2009) 3902–3914. `doi:https://doi.org/10.1016/j.cma.2009.08.013`.

[28] J. Kiendl, Y. Bazilevs, M.-C. Hsu, R. Wüchner, K.-U. Bletzinger, The bending strip method for isogeometric analysis of kirchhoff–love shell structures comprised of multiple patches, Computer Methods in Applied Mechanics and Engineering 199 (37) (2010) 2403–2416. `doi:https://doi.org/10.1016/j.cma.2010.03.029`.

[29] J. Kiendl, M.-C. Hsu, M. C. Wu, A. Reali, Isogeometric kirchhoff–love shell formulations for general hyperelastic materials, Computer Methods in Applied Mechanics and Engineering 291 (2015) 280–303. `doi:https://doi.org/10.1016/j.cma.2015.03.010`.

[30] G. Francfort, J.-J. Marigo, Revisiting brittle fracture as an energy minimization problem, Journal of the Mechanics and Physics of Solids 46 (8) (1998) 1319 – 1342. `doi:https://doi.org/10.1016/S0022-5096(98)00034-9`.

[31] B. Bourdin, G. Francfort, J.-J. Marigo, Numerical experiments in revisited brittle fracture, Journal of the Mechanics and Physics of Solids 48 (4) (2000) 797 – 826. `doi:https://doi.org/10.1016/S0022-5096(99)00028-9`.

[32] L. Ambrosio, A. Braides, Energies in sbv and variational models in fracture mechanics. (1997).

[33] J.-Y. Wu, V. P. Nguyen, C. T. Nguyen, D. Sutula, S. Sinaie, S. P. Bordas, Chapter one - phase-field modeling of fracture, Vol. 53 of Advances in Applied Mechanics, Elsevier, 2020, pp. 1–183. `doi:https://doi.org/10.1016/bs.aams.2019.08.001`.

[34] M. Dittmann, F. Aldakheel, J. Schulte, P. Wriggers, C. Hesch, Variational phase-field formulation of non-linear ductile fracture, Computer Methods in Applied Mechanics and Engineering 342 (2018) 71 – 94. `doi:https://doi.org/10.1016/j.cma.2018.07.029`.
URL `http://www.sciencedirect.com/science/article/pii/S0045782518303621`

[35] C. Miehe, D. Kienle, F. Aldakheel, S. Teichtmeister, Phase field modeling of fracture in porous plasticity: A variational gradient-extended eulerian framework for the macroscopic analysis of ductile failure, Computer Methods in Applied Mechanics and Engineering 312 (2016) 3 – 50, phase Field Approaches to Fracture. `doi:https://doi.org/10.1016/j.cma.2016.09.028`.
URL `http://www.sciencedirect.com/science/article/pii/S0045782516305412`

[36] A. Dean, S. Sahraee, J. Reinoso, R. Rolfes, A new invariant-based thermo-plastic model for finite deformation analysis of short fibre reinforced composites: Development and numerical aspects, Composites Part B: Engineering 125 (2017) 241–258.

[37] R. Alessi, F. Freddi, Phase-field modelling of failure in hybrid laminates, Composite Structures 181 (2017) 9 – 25. `doi:10.1016/j.compstruct.2017.08.073`.

[38] J. Bleyer, R. Alessi, Phase-field modeling of anisotropic brittle fracture including several damage mechanisms, Computer Methods in Applied Mechanics and Engineering 336 (2018) 213 – 236. `doi:https://doi.org/10.1016/j.cma.2018.03.012`.

[39] A. Quintanas-Corominas, J. Reinoso, E. Casoni, A. Turon, J. Mayugo, A phase field approach to simulate intralaminar and translaminar fracture in long fiber composite materials, Composite Structures (2019). `doi:10.1016/j.compstruct.2019.02.007`.

[40] T. Guillén-Hernández, I. G. García, J. Reinoso, M. Paggi, A micromechanical analysis of inter-fiber failure in long reinforced composites based on the phase field approach of fracture combined with the cohesive zone model, International Journal of Fracture (2019). `doi:10.1007/s10704-019-00384-8`.
URL `https://doi.org/10.1007/s10704-019-00384-8`

[41] A. Dean, J. Reinoso, N. Jha, E. Mahdi, R. Rolfes, A phase field approach for ductile fracture of short fibre reinforced composites, Theoretical and Applied Fracture Mechanics 106 (2020) 102495. `doi:https://doi.org/10.1016/j.tafmec.`

2020.102495.
URL http://www.sciencedirect.com/science/article/pii/S0167844219306536

[42] F. Alkhatib, E. Mahdi, A. Dean, Development of composite double-hat energy absorber device subjected to traverser loads, Composite Structures 240 (2020) 112046. doi:https://doi.org/10.1016/j.compstruct.2020.112046.
URL https://www.sciencedirect.com/science/article/pii/S0263822319345192

[43] M. Brod, A. Dean, S. Scheffler, C. Gerendt, R. Rolfes, Numerical modeling and experimental validation of fatigue damage in cross-ply cfrp composites under inhomogeneous stress states, Composites Part B: Engineering 200 (2020) 108050. doi:https://doi.org/10.1016/j.compositesb.2020.108050.
URL https://www.sciencedirect.com/science/article/pii/S1359836820306624

[44] E. Martínez-Pañeda, A. Golahmar, C. F. Niordson, A phase field formulation for hydrogen assisted cracking, Computer Methods in Applied Mechanics and Engineering 342 (2018) 742 – 761. doi:https://doi.org/10.1016/j.cma.2018.07.021.
URL http://www.sciencedirect.com/science/article/pii/S0045782518303529

[45] P. Asur Vijaya Kumar, A. Dean, J. Reinoso, P. Lenarda, M. Paggi, Phase field modeling of fracture in functionally graded materials:γ-convergence and mechanical insight on the effect of grading, Thin-Walled Structures 159 (2021) 107234. doi:https://doi.org/10.1016/j.tws.2020.107234.
URL https://www.sciencedirect.com/science/article/pii/S0263823120311046

[46] Hirshikesh, S. Natarajan, R. K. Annabattula, E. Martínez-Pañeda, Phase field modelling of crack propagation in functionally graded materials, Composites Part B: Engineering 169 (2019) 239–248. doi:https://doi.org/10.1016/j.compositesb.2019.04.003.
URL https://www.sciencedirect.com/science/article/pii/S135983681930229X

[47] D. Proserpio, M. Ambati, L. De Lorenzis, J. Kiendl, Phase-field simulation of ductile fracture in shell structures, Computer Methods in Applied Mechanics and Engineering 385 (2021) 114019. doi:https://doi.org/10.1016/j.cma.2021.114019.

[48] R. G. Tangella, P. Kumbhar, R. K. Annabattula, Hybrid phase-field modeling of thermo-elastic crack propagation, International Journal for Computational Methods in Engineering Science and Mechanics 0 (0) (2021) 1–16. doi:10.1080/15502287.2021.1904462.

[49] H. Badnava, M. A. Msekh, E. Etemadi, T. Rabczuk, An h-adaptive thermo-mechanical phase field model for fracture, Finite Elements in Analysis and Design 138 (2018) 31–47. doi:https://doi.org/10.1016/j.finel.2017.09.003.

[50] T.-T. Nguyen, D. Waldmann, T. Q. Bui, Computational chemo-thermo-mechanical coupling phase-field model for complex fracture induced by early-age shrinkage and hydration heat in cement-based materials, Computer Methods in Applied Mechanics and Engineering 348 (2019) 1–28. doi:https://doi.org/10.1016/j.cma.2019.01.012.

[51] A. Dean, J. Reinoso, S. Sahraee, R. Rolfes, An invariant-based anisotropic material model for short fiber-reinforced thermoplastics: Coupled thermo-plastic formulation, Composites Part A: Applied Science and Manufacturing 90 (2016) 186–199. doi:https://doi.org/10.1016/j.compositesa.2016.06.015.

[52] W. Shu, I. Stanciulescu, Monolithic and staggered strategies using solid-shell formulations for nonlinear coupled thermoelasticity, Journal of Engineering Mechanics 145 (12) (2019) 04019095. doi:10.1061/(ASCE)EM.1943-7889.0001669.

[53] M. Harnau, K. Schweizerhof, About linear and quadratic "solid-shell" elements at large deformations, Computers & Structures 80 (9) (2002) 805–817. doi:https://doi.org/10.1016/S0045-7949(02)00048-2.

[54] S. Klinkel, W. Wagner, A geometrical non-linear brick element based on the eas-method, International Journal for Numerical Methods in Engineering 40 (24) (1997) 4529–4545. doi:https://doi.org/10.1002/(SICI)1097-0207(19971230)40:24<4529::AID-NME271>3.0.CO;2-I.

[55] C. Miehe, A theoretical and computational model for isotropic elastoplastic stress analysis in shells at large strains, Computer Methods in Applied Mechanics and Engineering 155 (3) (1998) 193–233. doi:https://doi.org/10.1016/S0045-7825(97)00149-7.

[56] J. Reinoso, A. Blázquez, Application and finite element implementation of 7-parameter shell element for geometrically nonlinear analysis of layered cfrp composites, Composite Structures 139 (2016) 263–276. doi:https://doi.org/10.1016/j.compstruct.2015.12.009.

[57] M. Schwarze, S. Reese, A reduced integration solid-shell finite element based on the eas and the ans concept—large deformation problems, International Journal for Numerical Methods in Engineering 85 (3) (2011) 289–329. doi:https://doi.org/10.1002/nme.2966.

[58] P. Betsch, F. Gruttmann, E. Stein, A 4-node finite shell element for the implementation of general hyperelastic 3d-elasticity at finite strains, Computer Methods in Applied Mechanics and Engineering 130 (1) (1996) 57–79. doi:https://doi.org/10.1016/0045-7825(95)00920-5.

[59] M. Braun, M. Bischoff, E. Ramm, Nonlinear shell formulations for complete three-dimensional constitutive laws including composites and laminates, Computational Mechanics 15 (1) (1994) 1–18. doi:10.1007/BF00350285.

[60] K.-J. Bathe, E. N. Dvorkin, A four-node plate bending element based on mindlin/reissner plate theory and a mixed interpolation, International Journal for Numerical Methods in Engineering 21 (2) (1985) 367–383. doi:https://doi.org/10.1002/nme.1620210213.

[61] M. Bischoff, E. Ramm, Shear deformable shell elements for large strains and rotations, International Journal for Numerical Methods in Engineering 40 (23) (1997) 4427–4449. doi:https://doi.org/10.1002/(SICI)1097-0207(19971215)40:23<4427::AID-NME268>3.0.CO;2-9.

[62] R. Hauptmann, K. Schweizerhof, S. Doll, Extension of the 'solid-shell' concept for application to large elastic and large elastoplastic deformations, International Journal for Numerical Methods in Engineering 49 (9) (2000) 1121–1141. doi:https://doi.org/10.1002/1097-0207(20001130)49:9<1121::AID-NME130>3.0.CO;2-F.

[63] C. Miehe, A theoretical and computational model for isotropic elastoplastic stress analysis in shells at large strains, Computer Methods in Applied Mechanics and Engineering 155 (3) (1998) 193–233. doi:https://doi.org/10.1016/

S0045-7825(97)00149-7.

[64] R. Hauptmann, K. Schweizerhof, A systematic development of 'solid-shell' element formulations for linear and non-linear analyses employing only displacement degrees of freedom, International Journal for Numerical Methods in Engineering 42 (1) (1998) 49–69. doi:https://doi.org/10.1002/(SICI)1097-0207(19980515)42:1<49::AID-NME349>3.0.CO;2-2.

[65] J. Korelc, P. Wriggers, Consistent gradient formulation for a stable enhanced strain method for large deformations, Engineering Computations 13 (1) (1996) 103–123. doi:10.1108/02644409610111001.

[66] J. Simo, F. Armero, R. Taylor, Improved versions of assumed enhanced strain tri-linear elements for 3d finite deformation problems, Computer Methods in Applied Mechanics and Engineering 110 (3) (1993) 359–386. doi:https://doi.org/10.1016/0045-7825(93)90215-J.

[67] J. C. Simo, M. S. Rifai, A class of mixed assumed strain methods and the method of incompatible modes, International Journal for Numerical Methods in Engineering 29 (8) (1990) 1595–1638. doi:https://doi.org/10.1002/nme.1620290802.

[68] R. A. F. Valente, R. M. N. Jorge, R. P. R. Cardoso, J. M. A. César de Sá, J. J. A. Grácio, On the use of an enhanced transverse shear strain shell element for problems involving large rotations, Computational Mechanics 30 (4) (2003) 286–296. doi:10.1007/s00466-002-0388-x.

[69] P. Betsch, E. Stein, An assumed strain approach avoiding artificial thickness straining for a non-linear 4-node shell element, Communications in Numerical Methods in Engineering 11 (11) (1995) 899–909. doi:https://doi.org/10.1002/cnm.1640111104.

[70] E. N. Dvorkin, K. Bathe, A continuum mechanics based four-node shell element for general non-linear analysis, Engineering Computations 1 (1) (1984) 77–88. doi:10.1108/eb023562.

[71] L. Adam, J.-P. Ponthot, Thermomechanical modeling of metals at finite strains: First and mixed order finite elements, International Journal of Solids and Structures 42 (21) (2005) 5615–5655, pACAM VIII SPECIAL ISSUE. doi:https://doi.org/10.1016/j.ijsolstr.2005.03.020.

[72] R. P. R. Cardoso, J. W. Yoon, M. Mahardika, S. Choudhry, R. J. Alves de Sousa, R. A. Fontes Valente, Enhanced assumed strain (eas) and assumed natural strain (ans) methods for one-point quadrature solid-shell elements, International Journal for Numerical Methods in Engineering 75 (2) (2008) 156–187. doi:https://doi.org/10.1002/nme.2250.

[73] F. Gruttmann, W. Wagner, Structural analysis of composite laminates using a mixed hybrid shell element, Computational Mechanics 37 (6) (2006) 479–497. doi:10.1007/s00466-005-0730-1.

[74] E. P. Kasper, R. L. Taylor, A mixed-enhanced strain method: Part ii: Geometrically nonlinear problems, Computers & Structures 75 (3) (2000) 251–260. doi:https://doi.org/10.1016/S0045-7949(99)00135-2.

[75] G. Hütter, Coleman–Noll Procedure for Classical and Generalized Continuum Theories, Springer Berlin Heidelberg, Berlin, Heidelberg, 2017, pp. 1–8. doi:$10.1007/978-3-662-53605-6_57-1$.

[76] C. Kuhn, A. Schlüter, R. Müller, On degradation functions in phase field fracture models, Computational Materials Science 108 (2015) 374 – 384, selected Articles from Phase-field Method 2014 International Seminar. doi:https://doi.org/10.1016/j.commatsci.2015.05.034.

[77] C. Kuhn, R. Müller, A continuum phase field model for fracture, Engineering Fracture Mechanics 77 (18) (2010) 3625 – 3634. doi:https://doi.org/10.1016/j.engfracmech.2010.08.009.

[78] A. Mesgarnejad, B. Bourdin, M. Khonsari, Validation simulations for the variational approach to fracture, Computer Methods in Applied Mechanics and Engineering 290 (2015) 420 – 437. doi:https://doi.org/10.1016/j.cma.2014.10.052.

[79] P. K. Kristensen, E. Martínez-Pañeda, Phase field fracture modelling using quasi-newton methods and a new adaptive step scheme, Theoretical and Applied Fracture Mechanics 107 (2020) 102446. doi:https://doi.org/10.1016/j.tafmec.2019.102446.

[80] Y. Navidtehrani, C. Betegón, E. Martínez-Pañeda, A simple and robust abaqus implementation of the phase field fracture method, Applications in Engineering Science 6 (2021) 100050. doi:https://doi.org/10.1016/j.apples.2021.100050.

[81] P. K. Kristensen, C. F. Niordson, E. Martínez-Pañeda, An assessment of phase field fracture: crack initiation and growth, Philosophical Transactions of the Royal Society A: Mathematical, Physical and Engineering Sciences 379 (2203) (2021) 20210021. doi:10.1098/rsta.2021.0021.

[82] Z. Khalil, A. Y. Elghazouli, E. Martínez-Pañeda, A generalised phase field model for fatigue crack growth in elastic–plastic solids with an efficient monolithic solver, Computer Methods in Applied Mechanics and Engineering 388 (2022) 114286. doi:https://doi.org/10.1016/j.cma.2021.114286.

[83] G. Molnár, A. Gravouil, 2d and 3d abaqus implementation of a robust staggered phase-field solution for modeling brittle fracture, Finite Elements in Analysis and Design 130 (2017) 27–38. doi:https://doi.org/10.1016/j.finel.2017.03.002.

[84] C. Miehe, L.-M. Schänzel, Phase field modeling of fracture in rubbery polymers. part i: Finite elasticity coupled with brittle failure, Journal of the Mechanics and Physics of Solids 65 (2014) 93–113. doi:https://doi.org/10.1016/j.jmps.2013.06.007.

[85] M. Munoz, M. Alonso-García, N. Vela, F. Chenlo, Early degradation of silicon pv modules and guaranty conditions, Solar Energy 85 (9) (2011) 2264–2274. doi:https://doi.org/10.1016/j.solener.2011.06.011.

[86] A. Sapora, M. Paggi, A coupled cohesive zone model for transient analysis of thermoelastic interface debonding, Computational Mechanics 53 (4) (2014) 845–857. doi:10.1007/s00466-013-0934-8.

[87] M. Paggi, A. Sapora, Numerical modelling of microcracking in pv modules induced by thermo-mechanical loads, Energy Procedia 38 (2013) 506–515, proceedings of the 3rd International Conference on Crystalline Silicon Photovoltaics (SiliconPV 2013). doi:https://doi.org/10.1016/j.egypro.2013.07.310.